Chemical Geology 609 (2022) 121060

Contents lists available at ScienceDirect

Chemical Geology

journal homepage: www.elsevier.com/locate/chemgeo

Rapid alteration of cortical bone in fresh- and seawater solutions visualized and quantified from the millimeter down to the atomic scale

Anna G. Kral [a,*], Markus Lagos [a], Paul Guagliardo [b], Thomas Tütken [c], Thorsten Geisler [a]

[a] Institut für Geowissenschaften, Rheinische Friedrich-Wilhelms-Universität, Poppelsdorfer Schloss, Meckenheimer Allee 169, 53115 Bonn, Germany
[b] Centre for Microscopy, Characterization and Analysis, The University of Western Australia, 35 Stirling Highway, Perth, WA 6009, Australia
[c] Institut für Geowissenschaften, Johannes-Gutenberg-Universität, Johann-Joachim-Becher-Weg 21, 55128 Mainz, Germany

ARTICLE INFO

Editor: Claudia Romano

Keywords:
bioapatite
early diagenesis
nanoSIMS
cortical bone
ICP-MS
Raman spectroscopy
aqueous alteration
EMPA

ABSTRACT

It is widely known that *post mortem* diagenetic alteration processes cause modifications and overprinting of the chemical and isotopic proxies incorporated *in vivo* in bone apatite and collagen. Understanding the processes occurring during the interaction between fluids and bones in an early diagenetic setting is fundamental to determining the extent to which the commonly-used geochemical proxies in bone get modified during fossilization. The present study experimentally investigates the structural and chemical changes in bone induced by controlled *in vitro* aqueous alteration experiments under simulated early diagenetic conditions. It is intended to derive a deeper phenomenological and quantitative understanding of the transport and reaction processes that occur in the early stage of fossilization. For this purpose, 3.5 mm-sized cylinders were drilled from modern ostrich cortical bone and immersed in different experimental solutions enriched with tracers such as Zn, Sr, rare earth elements, and U. The experiments ran for several hours to weeks at 30, 60, and 90 °C - the latter two temperatures were chosen to accelerate anticipated early diagenetic modifications of the bone samples. Both the bone samples and the experimental solutions were analyzed using micro-analytical techniques such as Raman spectroscopy, electron microprobe, high-resolution inductively coupled plasma-mass spectrometry, nanoscale ion microprobe, and atom probe tomography to assess mineralogical, chemical, and structural changes from the millimeter to the atomic scale. The results show that element uptake into the bone samples occurs within hours after they have been exposed to an aqueous solution instead of years, as previously assumed. Additionally, distinct modifications of the organic phase were observed, accompanied by the growth of new apatite phases by dissolution-reprecipitation and recrystallization processes. Carbonate-poor or -free hydroxylapatite formed in the sample center and more stable carbonated fluorapatite in the sample rim. From these data, a phenomenological model is derived that explains the interaction between bone and aqueous solutions during the earliest stages of fossilization. This study also demonstrates the importance of using a comprehensive methodological approach when investigating alteration processes whose effects range from the millimeter down to the atomic scale.

1. Introduction

Investigating the uptake of major, trace, and rare earth elements (REEs) in fossil bone during diagenesis and the associated changes in its original chemical and isotopic composition (Henderson et al., 1983; Williams et al., 1997) provides valuable information about *post mortem* environmental conditions and processes (e.g., Wang and Cerling, 1994; Nielsen-Marsh and Hedges, 2000; Trueman and Tuross, 2002; Pucéat et al., 2004; Trueman et al., 2008; Herwartz et al., 2013; Reynard and Balter, 2014; Tacail et al., 2020). Bones are mineralized tissues composed of meta-stable nano-crystalline bioapatite, collagenous proteins, and water (Glimcher, 2006; Boskey and Robey, 2013; Grandfield et al., 2018; Reznikov et al., 2018). Bioapatite, the main constituent of bone, is a calcium phosphate mineral ($Ca_{10-x}[(PO_4)_{6-x}(CO_3)_x](OH)_{2-x}{\cdot}nH_2O$, Pasteris et al., 2014) that can incorporate a large number of elements and molecules. On the one hand, this property renders

Abbreviations: nanoSIMS, nanoscale secondary ion mass spectrometry; ICP-MS, inductively coupled plasma-mass spectrometry; EMPA, electron microprobe analysis.

* Corresponding author.
E-mail addresses: akral@uni-bonn.de (A.G. Kral), mlagos@uni-bonn.de (M. Lagos), paul.guagliardo@uwa.edu.au (P. Guagliardo), tuetken@uni-mainz.de (T. Tütken), tgeisler@uni-bonn.de (T. Geisler).

https://doi.org/10.1016/j.chemgeo.2022.121060
Received 13 January 2022; Received in revised form 15 July 2022; Accepted 10 August 2022
Available online 14 August 2022

bioapatite a valuable source of chemical and isotopic information for reconstructing, for example, ancient and modern climate and living conditions (e.g., Longinelli, 1984; Hedges et al., 2004; Levin et al., 2006), diet (e.g., DeNiro and Epstein, 1978, 1981; Schoeninger and DeNiro, 1984; Wang and Cerling, 1994; Fogel and Tuross, 2003; Scott and Poulson, 2012; Jaouen et al., 2013; Davis and Pineda-Munoz, 2016; Bourgon et al., 2020), or provenance and migration patterns (e.g., Ericson, 1985; Hoppe et al., 1999; Beard and Johnson, 2000; Taylor et al., 2019; Guiry et al., 2020; Kowalik et al., 2020; Monti et al., 2021). However, on the other hand, the same properties and its nano-crystalline nature make bioapatite prone to *post mortem* diagenetic alteration induced by changes in the physical and chemical environment. For example, pseudomorphic replacement of bioapatite can lead to modifications and overprinting of the bone's *in vivo* chemical and isotopic composition, while the original morphology may still be preserved (Kolodny et al., 1996; Pasteris and Ding, 2009). The ability to retain the fine-scale morphology during a mineral replacement process was demonstrated, for example, by an experimental study by Kasioptas et al. (2010). These authors experimentally pseudomorphically replaced the filigree, micrometer-sized, chamber-like architecture of squid cuttlebone (*Sepia officinalis* Linnaeus, 1758), made of aragonite, in aqueous solutions with hydroxylapatite (HAp) and a small amount of ß-tricalcium phosphate. They explained the replacement by an interface-coupled dissolution-precipitation process following the notion of Putnis (2002). Therefore, the need arises to differentiate between chemical and isotopic information incorporated *in vivo* versus that information altered by *post mortem* taphonomic processes. *Post mortem* modifications depend on the diagenetic environment (e.g., Kohn et al., 1999; Collins et al., 2002; Hedges, 2002; Jans, 2008; Karr and Outram, 2012; Matthiesen et al., 2021) but also on the susceptibility of individual elements for diagenetic mobilization (Martin et al., 2017 and references therein). Thus, a thorough understanding of how the chemical and isotopic composition of bone can be affected in different diagenetic settings by the alteration processes shortly after the death of the individuum is essential.

A variety of studies have systematically investigated the effect of diagenesis on the chemical and isotopic composition in bones and teeth (e.g., DeNiro, 1985; Trueman et al., 2004; Sponheimer and Lee-Thorp, 2006; Fricke et al., 2008; Hinz and Kohn, 2010; Herwartz et al., 2011; Heuser et al., 2011; Tütken and Vennemann, 2011; Tütken et al., 2011; Trueman, 2013; Tütken, 2014; Bourgon et al., 2020; Suarez and Kohn, 2020). Most of these studies focused on diagenetically altered archeological or fossilized bones, while systematic alteration experiments using modern bones or teeth covering the first days to years after death are scarce. Long-term burial experiments in wetland soils with modern alligator bones performed by Keenan and Engel (2017) showed that compositional alteration and distinct bioerosion were monitored after one week. In mesocosm experiments, microbial colonization was inhibited and transformation from bioapatite to a more stable apatite phase was observed after one month. Kohn and Moses (2012) conducted aqueous alteration experiments on bones to determine experimentally induced diffusion coefficients at 20 °C for numerous trace elements, including Sr, Zn, U, and REEs. This study showed that common charge-coupled element species limit the diffusion rate in bone and led to similarities in diffusion rates. Consequently, trace element profiles in fossilized bone were unlikely to be caused by intra-bone volume diffusion as formerly assumed, but presumably due to recrystallization and transport limitations. Moreover, aqueous alteration experiments, in which calcined bone and tooth enamel were exposed to ^{87}Sr-doped solutions for one year, showed that the ability to incorporate Sr into the apatite crystal lattice is considerably smaller for bones or teeth with high apatite crystallinity (Snoeck et al., 2015).

Another controlled alteration study with modern bone in aqueous NaF solution at pH 9–10 for up to three weeks at maximum temperatures of 70 °C was performed by Aufort et al. (2019). The authors proposed a transformation mechanism that involves the partial dissolution of bioapatite as well as reprecipitation of secondary apatite, which occurs irrespective of the presence or absence of F, thus leading to the formation of carbonate-bearing fluorapatite (FAp) and/or HAp, respectively.

Furthermore, Turner-Walker and Peacock (2008) conducted long-term, real-time field experiments on bovine bone and pig skin in Scandinavian bogs, representing an acidic environment, to model the formation of a bog body. Notably, in *Sphagnum* bogs, bone was not affected by bioerosion, but mineral leaching and extensive demineralization were observed after one year. This eventually exposes the collagen matrix, which shrinks upon drying and leads to the formation of cracks in the bone. Similar observations were made in a comprehensive study of time-resolved aqueous alteration of dental cubes from modern elephant teeth under controlled conditions representing an extremely acidic early diagenetic environment (Weber et al., 2021). In the outer parts of dentin samples from low-temperature (30 °C) experiments, partial dissolution of the apatite component occurred after only four days, while the organic material was preserved in such a specific acidic environment. This study also showed that the Ca, Sr, Zn and Mg isotopic compositions in dentin were strongly influenced by diagenetic modification. In contrast, only the outermost 100–300 μm of enamel were affected by the changes, while the central part of the mm-thick enamel remained unaltered. Kral et al. (2021) used a similar experimental approach in an *in vitro* aqueous alteration study on modern ostrich cortical bone (CB) mimicking natural aquatic early diagenetic conditions to study their effect on CB microarchitecture. The CB samples were experimentally altered in fresh- and seawater-like solutions (FW and SW, respectively) at 30 °C as well as 60 and 90 °C in order to accelerate bone aging. This study showed that the CB microarchitecture remained largely resistant to aqueous alteration on a microscopic scale. However, in CB samples altered in FW solutions, an unevenly distributed reaction rim (RR) was detected within the outermost layer demonstrating a strong influence of the solution chemistry on the alteration.

The results of the present study expand on and complement the results obtained by Kral et al. (2021). To this end, the same cylindric bone samples and the respective experimental solutions altered at 30 to 90 °C were analyzed using various micro-analytical techniques to assess mineralogical, chemical, and structural changes from the millimeter down to the atomic scale. The 30 °C temperature regime is typical for early diagenetic pre-burial or near-Earth surface postdepositional aqueous or sedimentary settings. Temperature ranges up to 60 °C are known to accelerate bone aging artificially and thus the reaction and transport processes, however, without denaturing even unmineralized collagen (Waite et al., 1997; Dobberstein et al., 2009; Abdel-Maksoud, 2010; Turner-Walker, 2011). Although experiments at 90 °C are not typical for most early diagenetic settings, they allow for predictions of processes that may occur over longer time intervals assuming that elevated temperature compensates for shorter reaction durations. Mineralized collagen has a distinctly higher thermal stability than unmineralized collagen. The endothermic transition is shifted from 60 °C in unmineralized collagen to up to 150 °C in mineralized collagen (Kronick and Cooke, 1996). It can therefore be assumed that, even in the 90 °C experiments, the processes are only greatly accelerated, but no new processes are triggered that would not have occurred, albeit much later, at 30 or 60 °C. The results of these experiments probably cannot be directly linked to specific early diagenetic settings - which is not the intent of this study - but they do provide insights into how both the mineral and collagen phases can be altered after longer periods of time of burial and diagenesis in the geological record.

The analytical approach was to study the samples from the macroscopic down to the atomic level, with the analyses building on each other: micro-computed tomography (μCT) data of the reacted CB samples were used to define the areas of interest (such as the RRs), which were then further investigated by electron microprobe analysis (EMPA) chemical imaging, which, in turn, delivered the basis for selecting samples and sample areas of interest for nanoscale secondary ion mass spectrometry (nanoSIMS) isotope mapping at the sub-μm resolution,

which has so far not been applied to modern or fossilized bone. These bone tissue data were supplemented with quantitative analyses of the initial and final solutions of the respective *in vitro* alteration experiments using high-resolution inductively coupled plasma-mass spectrometry (HR-ICP-MS). In addition, confocal Raman spectroscopy was used to investigate potential alteration effects on the organic and inorganic components of the CB samples. Finally, atom probe tomography (APT) was applied to visualize and quantify changes in element distribution in three dimensions (3D) from the millimeter down to the atomic scale. With this approach, the study aims to gain more insights into the interaction between CB and aqueous fluids and derive a more detailed phenomenological and quantitative understanding of the transport and reaction processes active during the earliest stage of fossilization.

2. Materials and methods

2.1. Experimental setup

All experimental run products analyzed here originated from *in vitro* aqueous alteration experiments of a recently conducted study to assess changes in bone microstructure (Kral et al., 2021). Detailed information on the CB samples, the preparation of the experimental solutions, and the experimental setup can be found therein and in Appendix 1. Briefly, the cylindric CB samples (Fig. 1A) were drilled (3.5 mm × 3.5 mm cores)

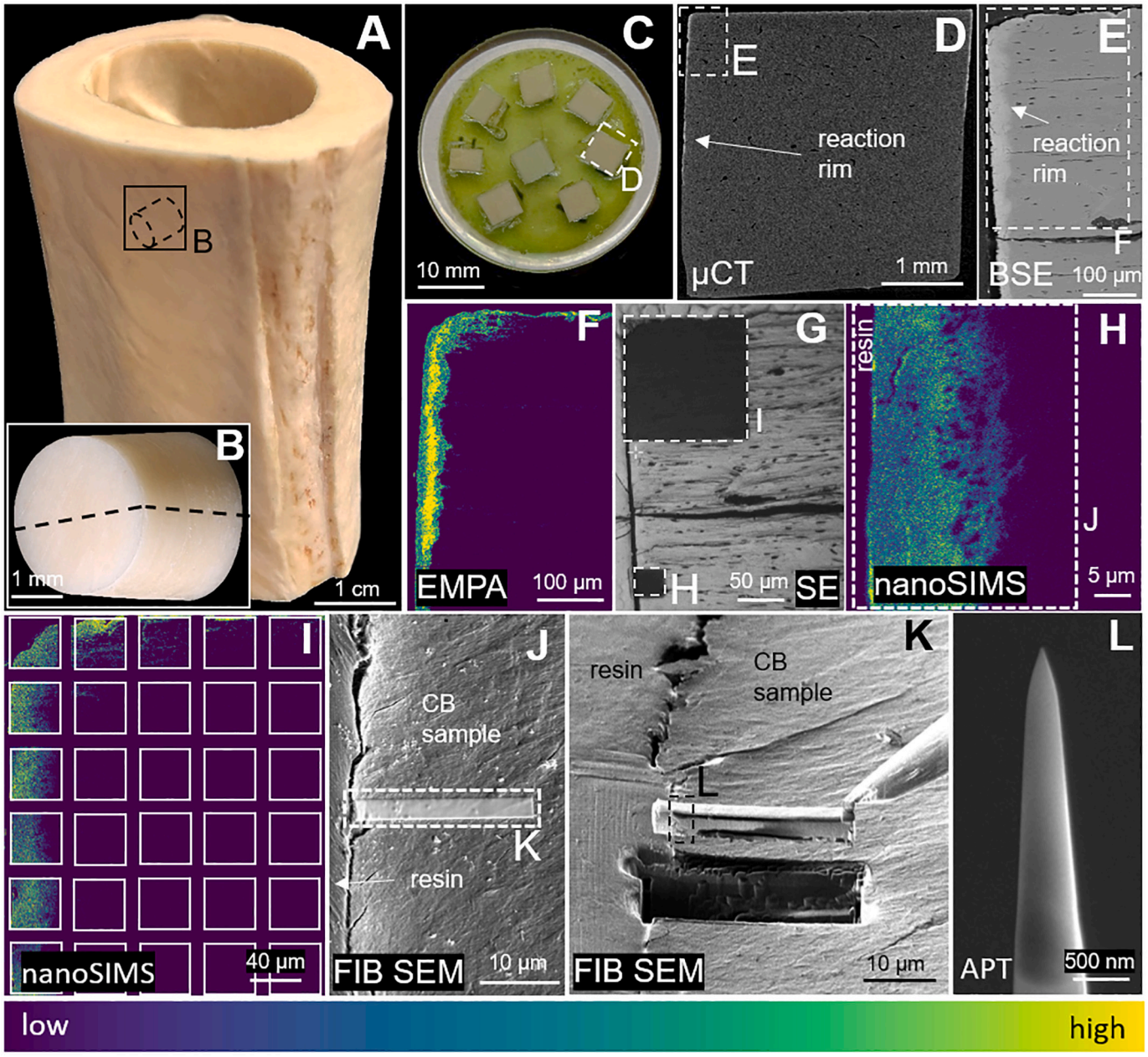

Fig. 1. Methodological overview of chemical analysis of *in vitro* altered bone at different spatial scales. (A) The cortex of the diaphyseal part of the analyzed modern ostrich tibia. (B) Cylindric cortical bone drill core sample with dashed line indicating the cutting plane. (C) Representative mount with polished samples embedded in Technovit© resin. (D) Representative µCT section illustrating the bright RR and the selected area for EMPA and nanoSIMS. (E) Backscattered electron (BSE) image with the dashed lines indicatingthe selected area for EMPA. (F) Color-coded EMPA images displaying the U distribution. (G) Secondary electron image showing the localities of (H) a single nanoSIMS map and of (I) a mosaic image consisting of 30 individual nanoSIMS maps, both displaying the spatial distribution of U. (J) Secondary electron image of the area perpendicular to the sample's edge that was selected for APT and covered with platinum. (K) Extraction of an APT wedge that was later cut into five sections and (L) prepared in the form of a needle. The uniformly-scaled Viridis palette was used for color-coding the images.

Table 1
Element concentrations of freshwater (FW) and seawater (SW) stock solutions in ppm.

Cation/anion	FW	SW
B^{3+}	2.34 ± 0.06	3.15 ± 0.07
Na^{+}	*100.0 ± 0.2*	*10,770 ± 22*
K^{-}	*100.0 ± 0.2*	*390.0 ± 0.8*
Ca^{2+}	1426 ± 15	562 ± 6
Cl^{-}	*775 ± 2*	*19,350 ± 39*
Mg^{2+}	122.0 ± 1.4	859.2 ± 1.7
F^{-}	*5.00 ± 0.01*	*5.00 ± 0.01*
Sr^{2+}	137.6 ± 0.9	140.1 ± 1.9
Zn^{2+}		9.6 ± 0.5
Lu^{3+}	3.51 ± 0.01	
Nd^{3+}	1.754 ± 0.003	
U^{6+}	16.0 ± 0.2	

from the bone compacta of a single tibia from a five-year-old male modern ostrich (*Struthio camelus* Linnaeus, 1758) that was raised on an ostrich farm in Remagen, Germany. After drilling, the samples were rinsed with MQ water, air-dried under a laboratory fume hood, and scanned using μCT. After this pre-characterization, the dry samples were exposed to three types of aqueous solutions by putting one CB sample and 2 mL of a solution into 3 mL Teflon© vials, which were then placed in custom-made cold-sealed steel containers. These containers were kept in a custom-made oven under autogenous pressure (<5 bar) for up to 30 d at 30, 60, and 90 °C. The solutions were not stirred during the experiment. The more elevated temperatures of 60 and 90 °C were applied to accelerate the reaction and transport processes (Dobberstein et al., 2009; Abdel-Maksoud, 2010; Turner-Walker, 2011). After terminating the experiments, the samples were rinsed three times with MQ water and air-dried under a laboratory fume hood at 21 °C. Only CB samples derived from two of the three experimental series were further investigated in the present study. These solutions had either a freshwater-like composition (FW), isotopically labeled with depleted U and enriched with Nd and Lu, with low salinity (≈ 1 g/kg) and a starting pH of 7.40 ± 0.06 at 21 °C or a seawater-like composition (SW), enriched with Zn only with a salinity of ≈ 30 g/kg and an initial pH of either 7.82 or 8.04 ± 0.06 at 21 °C (see Appendix 4 for details). These two solutions were used as model analogs of the most abundant types of aqueous solutions on Earth in which bones typically fossilize. The elements of particular interest were B, F, Mg, P, Ca, Zn, Sr, Nd, Lu, and U (see Table 1 for details), which are all commonly used for reconstructions of the paleoecology or taphonomy of vertebrates.

In total, CB samples of 30 experiments, the respective experimental solutions, three blanks comprised of MQ water as well as the three stock solutions were analyzed. To this end, the cylindric CB samples were cut into two half-round parts using an SP 1600 microtome (Leica Biosystems, Wetzlar, Germany) with the cut surface being oriented perpendicular to the longitudinal growth direction (Fig. 1B). During cutting, the saw blade and the CB samples were constantly cooled with water Afterwards, the CB samples were again air-dried under a laboratory fume hood at 21 °C. Following cutting, half of each CB sample was embedded in a standard mount using Technovit® 5071 resin (Kulzer Technik, Wehrheim, Germany) and the cutting surface was polished with a 1 μm diamond polishing agent (Fig. 1C).

The composition of the stock solution constituents B, Ca, Mg, Sr, Zn, Fe, Lu, Nd, and U [ppm ± SD] was determined using an Element 2/XR Sector Field ICP-MS system. For the remaining constituents, the concentration was calculated from the weight-in and is given in italic font [ppm ± 0.2%]. The weighted substances contained in both types of solution were B_2O_3, $NaHCO_3$, NaF, KCl, $CaCl_2$, $MgCl_2$, and $SrCl_2$, while the FW solution solely contained $FeCl_3$, $NdCl_3$, $LuCl_3$, and $UO_2(NO_3)_2$ and the SW solution NaCl, Na_2SO_4, $Ca(NO_3)_2$, and $ZnCl_2$.

2.2. Electron microprobe analysis

EMPA were performed using a JXA 8200 Superprobe (JEOL Ltd., Tokyo, Japan) with five wavelength-dispersive spectrometers and an energy-dispersive X-ray, a backscatter, and a cathodoluminescence detector. The polished sample mounts were coated with ≈ 20 nm of carbon. Suitable areas for analysis were selected based on μCT images acquired during sample pre-characterization (Fig. 1D). BSE images (Fig. 1E) and qualitative element distribution images with a point-by-point step size of 1 μm (Fig. 1F) were taken from an unaltered CB sample as well as from altered samples representative of the different solutions and reaction temperatures. For each BSE image, contrast and brightness were adjusted to achieve the maximum information about bone density changes. Therefore, comparisons of the greyscale levels between the images are only conditionally possible. The acceleration voltage was set to 15 keV at 15 nA beam current. Peak and background counting times were 10 s for all elements except for Na (5 s). The Kα-lines were used for F, Na, Mg, P, Cl, Ca, and Zn analysis, whereas the Mα line was used for U and the Lα line for Sr as well as the REEs Nd and Lu. The standards used for calibration were magmatic fluorapatite for P and Ca, magnesium oxide for Mg, and natural uraninite for U. Smithsonian microbeam references NMNH 133868 (anorthoclase, Jarosewich et al., 1980) and NMNH 10065 (strontianite, Jarosewich and White, 1987) were used for Na and Sr calibration, respectively. The REE orthophosphate $NdPO_4$ (USNM 168492) and $LuPO_4$ (USNM 168491) reference samples were used as standards for Nd and Lu quantification (Jarosewich and Boatner, 1991; Donovan et al., 2003). The ZAF matrix corrections were applied to correct peak intensities for backscattered electron loss, absorption, and secondary fluorescence effects (Philibert and Tixier, 1968; Goldstein et al., 1992).

2.3. Nanoscale secondary ion mass spectrometry

The nanoSIMS 50L system (Cameca, Gennevilliers, France) was used for qualitative elemental analysis. Mounts were coated with 10 nm of Au before analysis. Secondary electron imaging was used to locate target areas (Fig. 1G), previously determined using EMPA qualitative imaging. Before mapping, fields of view between 45 μm and 60 μm edge length were pre-sputtered using a current of 1 nA for 10 min. The isotope distribution maps obtained for B, F, Na, Mg, P, Ca, Zn, Sr, Nd, Lu, and U were displayed either as single nanoSIMS maps - each 40 × 40 μm^2 in size with 512 × 512 px in the sub-μm scale (Fig. 1H) - or as mosaic image consisting of a series of single nanoSIMS maps covering larger areas (Fig. 1I). Mappings acquired using a Cs^+ primary ion beam were located directly beside the previous maps scanned using an O^- ion beam to avoid charging effects and potential oxygen contamination caused by the ion beam. For imaging, the focused 16 keV Cs^+ primary ion beam with a lateral resolution of approximately 100 nm rastered a defined surface area to generate the negative ions $^{16}O^-$, $^{18}O^-$, $^{19}F^-$, $^{24}C^-$ ($^{12}C_2$), $^{26}N^-$ ($^{12}C^{14}N$), and $^{35}Cl^-$, while the O^- primary ion beam with a lateral resolution of approximately 200 nm was used to generate the positive ions $^{11}B^+$, $^{23}Na^+$, $^{24}Mg^+$, $^{31}P^+$, $^{40}Ca^+$, $^{67}Zn^+$, $^{88}Sr^+$, $^{142}Nd^+$, $^{175}Lu^+$, and $^{238}U^{16}O^+$. Seven different ion species were simultaneously detected. The most abundant isotope of each element was selected for the measurements because the experimental solutions were not isotopically enriched. The isotopic species will not be named in the following text, only the respective element. To collect and detect the secondary ions, an electrostatic and a magnetic sector were used. The O^- beam current was set to 50 pA, whereas the Cs^+ beam current was set to 4–5 pA - the eGun was used with the latter. Dwell times varied from 2.5 to 5 ms per pixel and multiple planes were recorded for each image. The obtained images were processed and large mosaic images were constructed using the software Fiji v1.53c with the plugins OpenMIMS (http://nano.bwh.havard.edu) and NRRD Mosaics (https://github.com/BWHCNI/OpenMIMS.wiki.git).

2.4. Atom probe tomography

Elemental and isotopic 3D compositional analyses were performed on the near-atomic scale on three representative CB samples using a CAMECA LEAP 4000X HR APT. To extract small sample volumes, an area of 2 μm × 20 μm traversing the RR was sputtered with Pt (Fig. 1J) using a TESCAN Lycra3 Ga^+ focused ion beam SEM (Rickard et al., 2020). The sputtered area was cut to a rectangular prism and removed using the *in situ* lift-out technique described by Thomas et al. (2007) (Fig. 1K). Each prism was cut into up to 10 segments with every segment being mounted on a post on pre-fabricated coupons and finally shaped needle-like by the ion beam (Fig. 1L). Detailed information on data acquisition and image reconstruction is provided elsewhere (Reddy et al., 2020).

2.5. Raman spectroscopy

Raman measurements were performed with a LabRam HR800 system (Horiba Scientific, France) equipped with a BX41 microscope (Olympus America Inc., Center Valley, PA, USA). Spectra were collected from CB samples ($n = 6$) that were treated for 30 d in FW and SW solutions at 30, 60, or 90 °C and pristine CB samples. For excitation of Raman scattering, a 200 mW diode-pumped solid-state laser (783.976 nm) was used, but only about 10% laser power reached the sample surface. The measurements were performed using a 100x objective with a numerical aperture of 0.9 and a confocal hole of 1000 μm. Before collection using an electron-multiplier charge-coupled device detector, the scattered Raman light passed through a 100 μm spectrometer entrance slit and was dispersed by a 600 grooves/mm grating. With these settings, the theoretical, diffraction-limited lateral and axial resolution was about 1 μm and <2 μm, respectively. At the beginning of each measurement session, the spectrometer was calibrated with the first-order band of a pure silicon standard at 520.7 cm^{-1}. Additionally, to correct for shifts during long-term analysis, the 886.19 cm^{-1} line of the laboratory room's ceiling light was used as an internal standard. The wavelength of this line was determined beforehand using the 985.43 cm^{-1} line of a neon lamp for which the wavelength is precisely known (Saloman and Craig, 2006). From the width of both lines, a spectral resolution of 1.94 ± 0.02 cm^{-1} was determined, which was used to correct the width of the Raman bands for finite slit width effects (Tanabe and Hiraishi, 1980). The analyses were performed along the sample's edge in the frequency range of 150–2000 cm^{-1} with an acquisition time of 20 s, two accumulations per spectrum, and a step size of 1 μm. The area covered by each analysis was slightly different depending on the individual sample structure. 41 single analyses were performed parallel to the sample edge, while the number of analyses perpendicular to the sample edge varied between 26 and 45. Spectra were also taken from multiple areas in the presumably less altered center of each sample. From all spectra, the parameters 'full width at half maximum' (FWHM) and the position of the $\nu_1(PO_4)$ fully symmetrical stretching band of apatite near 960 cm^{-1} were extracted by least-squares fitting. The $\nu_1(PO_4)$ band was fitted with an asymmetrical Gauss-Lorentz function to account for an asymmetry towards the low-frequency side observed in some bone apatite spectra. The procedure and reasoning have previously been described and discussed in more detail in Barthel et al. (2020), Geisler and Menneken (2021), and Weber et al. (2021).

2.6. High-resolution inductively coupled plasma-mass spectrometry

Concentrations of B, Mg, P, Ca, Zn, Sr, Nd, Lu, and U were determined by multi-element analyses of the experimental solutions using an Element 2/XR Sector Field ICP-MS system (Thermo Fisher Scientific, Waltham, MA, USA) equipped with a dual-mode secondary electron multiplier (counting and analog mode) combined with a Faraday detector. The three different detection modes allowed for a linear detection range over several orders of magnitude, which enabled analysis of the different experimental solutions with their strongly varying chemical and isotopic concentrations ranging from a few thousand ppm down to the ppt level.

Table 2
Overview of the analyzed isotopes and the applied mass resolution for the elements of interest (i.e., B, Mg, P, Ca, Zn, Sr, Nd, Lu, and U).

Element	Isotopes	Resolution
B	$^{10,11}B$	MR
Mg	$^{25,26}Mg$	MR
P	^{31}P	MR
Ca	^{43}Ca	MR
Zn	$^{66,68}Zn$	MR
Sr	^{88}Sr	LR
Nd	$^{143,146}Nd$	MR
Lu	^{175}Lu	MR, LR
U	^{238}U	LR

LR = low resolution, MR = medium resolution.

Every sequence started by rinsing the system using 2%-HNO_3, followed by 1) measuring five 2% HNO_3 blank solutions, 2) the calibration solutions (using a 5-point linear calibration based on several dilutions of the multi-element standard solution Merck Certipur VI, 3) several certified reference materials (SPS-SW2, SLRS-6, TM-26.4) which were used to validate the calibrations and 4) finally the sample solutions. After every tenth sample solution, a blank solution was analyzed for updated background correction. Before the measurement of each new sample, the sample introduction system was rinsed with 2% or 5%-HNO_3 for at least 2 min or until an appropriate background level was reached. The mean ($n = 2$), the standard deviation, and the relative standard deviation were calculated for each sample. Furthermore, the detection limit was determined and used to correct the results, which were additionally checked for plausibility. For analysis, aliquots were taken from all experimental solutions ($n = 30$), the stock solutions (n = 2) and from the experimental blanks (n = 3). Before diluting the experimental solutions, all aliquots were centrifuged for 10 min at 13,000 rpm to ensure that potential suspended matter had settled. The final dilution factor was determined via pre-scans and varied between 5-fold and 300,000-fold. 1 ppb of ^{103}Rh was added to all aliquots as an internal standard to correct for short-term instrumental drift. In addition, potential long-term instrumental drift was also investigated and corrected if necessary. This was done by repeatedly analyzing the calibration solutions throughout the analytical sequence.

Details about the analyzed isotopes as well as the applied resolution modes are given in Table 2. Measurements in medium resolution (MR) mode (mass resolution of 4000) were generally conducted to avoid signal contributions from potential polyatomic interfering species. Regarding elements that are often prone to interfering species (B, Mg, Zn, and Nd), the signal intensities of two different isotopes were recorded and compared. In the case of Mg, Zn, and Nd, results of both signal intensities agree within uncertainty and the mean of both was used for evaluation. For B however only signal intensities of ^{10}B were chosen for further evaluation because ^{11}B gave higher intensities presumably due to severe interference from $^{23}Na^{2+}$ which is also present in the sample solutions. Lu for instance was analyzed in low resolution (LR) as well as in MR mode. Both results agreed with uncertainty but for further evaluation, only the LR signal intensities were used because of higher precision and lower detection limits.

3. Results

3.1. Textural alteration

BSE images revealed an overall intact microstructure in pristine CB with few microcracks in the interstitial bone and only slight differences in greyscale intensities. The interstitial bone appeared slightly brighter than the osteonal bone (Fig. 2A). After the experiments, the intact CB

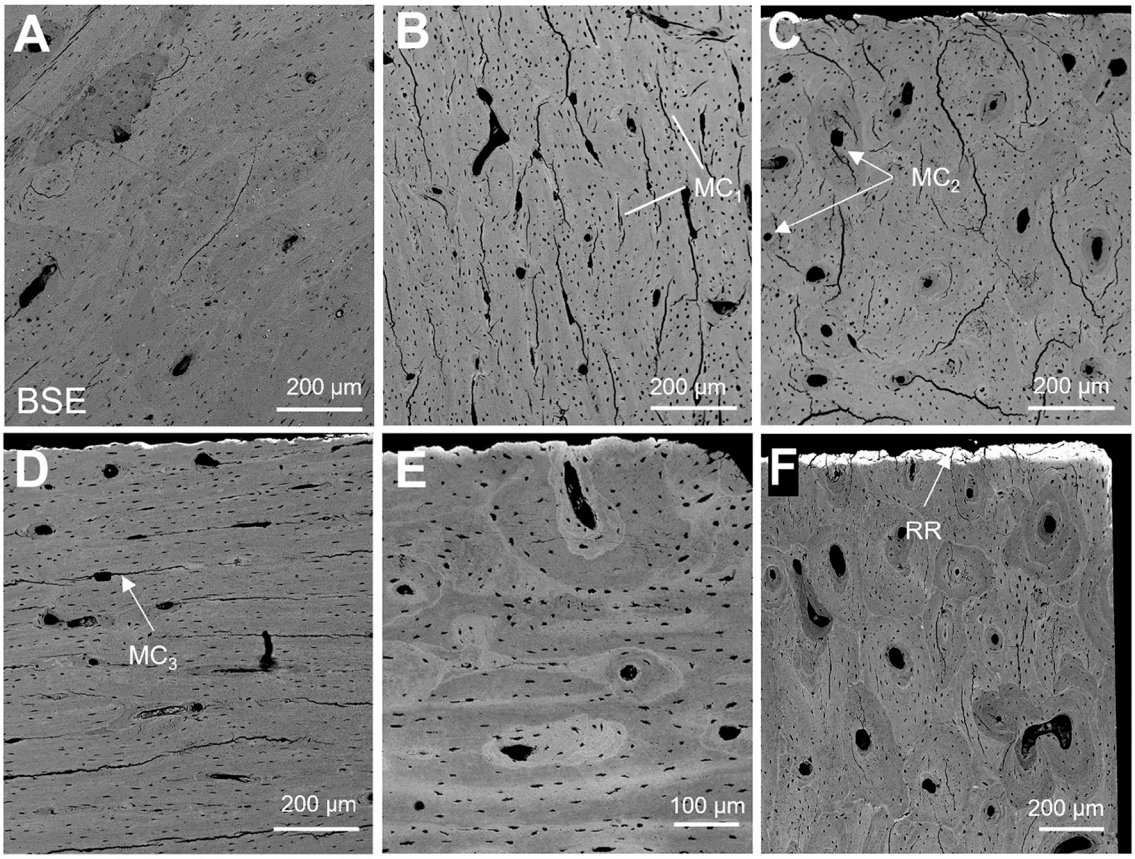

Fig. 2. Series of representative BSE images of cross-sections of (A) pristine and (B - F) altered cortical bone (CB) samples. Altered CB samples show experimentally induced microcracks of (B) type 1 (1 d at 30 °C in SW), (C) type 2 (1 d at 30 °C in FW) and, (D) type 3 (7 d at 90 °C in FW). See text for details. (E) CB sample without microcracks (30 d at 90 °C in FW). (F) CB sample with a pronounced reaction rim (RR) (3 d at 30 °C in FW).

was pervaded by experimentally induced microcracks, which were observed after 1 d, irrespective of the applied temperature or solution composition (Fig. 2B, C). The microcracks were only partially visible in the µCT virtual sections due to the lower resolution of the µCT scans (Appendix 2). The appearance of the cracks differed depending on the orientation of the CB sample during cutting. In CB samples cut perpendicular to the longitudinal growth direction, microcracks appeared relatively short in length (≈10 to 200 µm), not connected, and predominantly originated in the interstitial bone without any preferential orientation (MC_1 in Fig. 2B). Microcracks were also found within osteons, either entirely restricted to the osteon or connected with the interstitial bone, whereby the cement line was crossed (MC_2 in Fig. 2C) - no preferred orientation was observed for this type of microcrack either. In CB samples cut along the Haversian canals, microcracks were primarily located in the interstitial bone but did connect with an osteon at one or both sides. Moreover, these microcracks were oriented parallel to each other and reached lengths of up to several 100 µm (MC_3 in Fig. 2D). A tendency towards stronger greyscale variations, e.g., in osteonal bone, and a reduction in the number and length of microcracks was observed with increasing temperature and experimental duration (Fig. 2E). It was also found that CB samples immersed in FW solutions showed a bright (i.e., higher density), unevenly distributed area along the sample edge with a thickness of up to 20 µm (Fig. 2F), which was previously described and referred to as the reaction rim (RR) by Kral et al. (2021).

3.2. Chemical alteration

3.2.1. Micrometer-scale observations

Qualitative EMPA element distribution maps obtained from pristine CB samples revealed slightly unevenly distributed P (Fig. 3A) and Ca (Fig. 3B) at the micrometer scale. Mg (Fig. 3C), Na (Fig. 3D), and Sr (Fig. 3E) were evenly distributed, albeit close to the detection limit (0.01, 0.02, and 0.03 wt%, respectively). Element concentrations of Zn, Nd, Lu, and U were generally below the detection limit (0.05, 0.02, 0.07, and 0.02 wt%, respectively). CB samples experimentally altered in FW solutions at 60 °C were depleted in P, Ca, and Mg in the area of the RR to varying extent, but relative enriched further inside the sample (Fig. 3F, G, H, respectively). The spatial distribution of Na (Fig. 3I) did not differ significantly from that in pristine CB, irrespective of the experimental solution the CB was exposed to. Furthermore, in CB samples derived from FW experiments, Sr (Fig. 3J), Nd (Fig. 3K), Lu (Fig. 3L), and U (Fig. 3M) were concentrated within the RR to varying extent. Under 90 °C, these distribution patterns did not change notably, except for Ca, which was enriched along the sample's edge (Fig. 3N). However, this could also be an artifact of drying. Dissolved Ca ions could have been concentrated near the sample surface during air drying, even if the CB samples were rinsed several times to flush out the pore water enriched with dissolved ions. CB samples that reacted in SW solutions at 60 and 90 °C showed element distributions comparable to the FW sample, except for Mg and Zn. Magnesium was not significantly changed in its distribution, whereas Zn (Fig. 3O) appears to have been enriched along the edge of the sample. Note that Nd, Lu, and U were not included in the SW solution.

3.2.2. Nanometer-scale observations

To supplement the EMPA element distribution images with chemical/isotopic images of higher resolution, nanoSIMS imaging was used for the first time to chemically and isotopically characterize experimentally altered CB samples at the nanometer scale. In CB samples from both experimental series (FW, SW), the highest intensities of F were

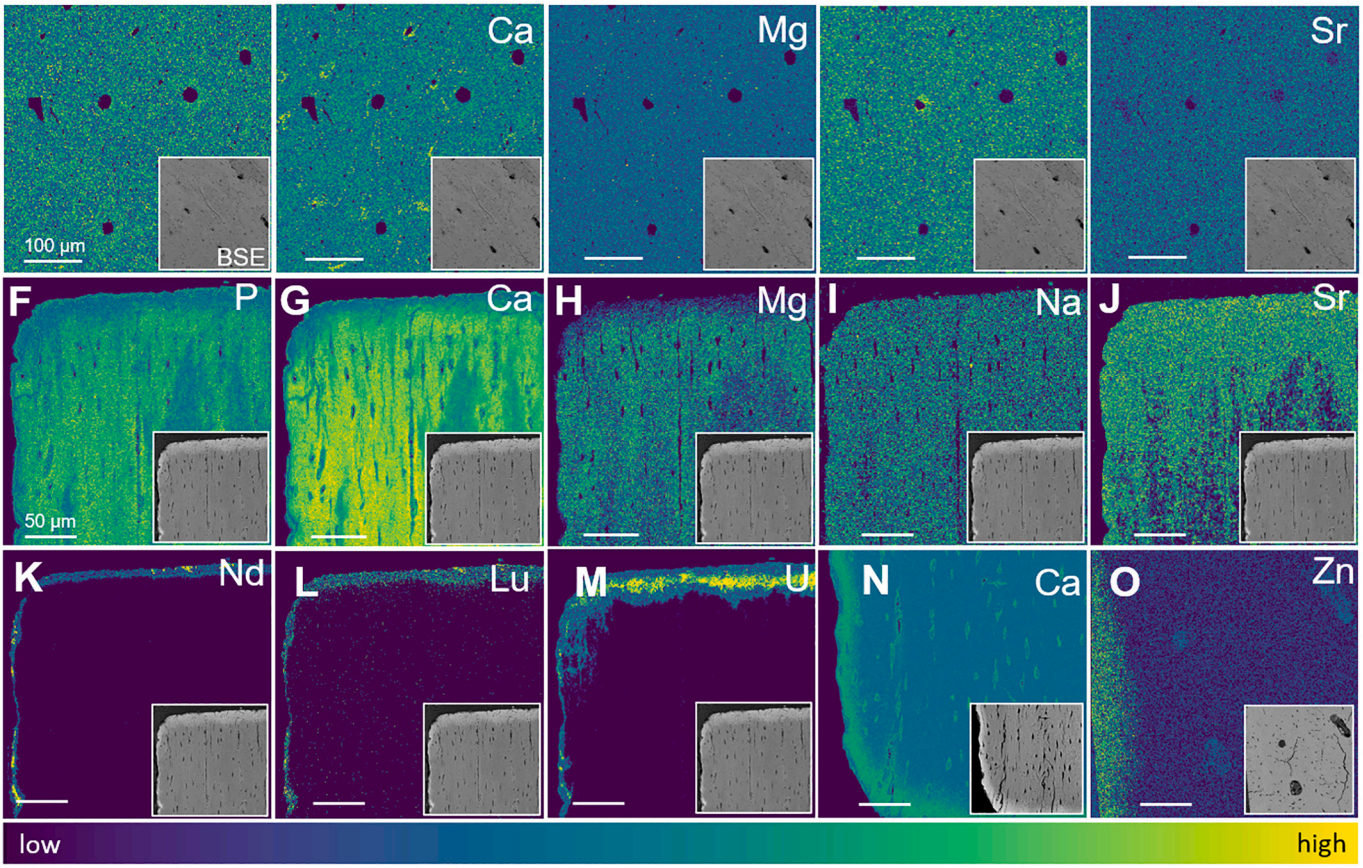

Fig. 3. EMPA element distribution maps of pristine and altered cortical bone (CB). Images A - E show pristine and images F - O altered CB (30 d at 60 or 90 °C) with inset maps representing BSE images with an edge length of 300 µm. (A - E) Distribution of P, Ca, Mg, Na, and Sr in unaltered CB, respectively. Images (F - M) display the P, Ca, Mg, Na, Sr, Nd, Lu, and U distribution, respectively, in samples reacted in FW at 60 °C. Similar distributions were observed in samples derived from SW experiments, except for Nd, Lu, and U. Image (N) is representative of the Ca distribution in samples reacted at 90 °C in FW and SW. (O) Zinc distribution in a sample exposed to SW – note that FW solutions did not contain Zn. Images A - E and F - O have the same scale bar of 100 µm and 50 µm, respectively.

measured in the outermost 20 µm of the samples (Fig. 4A, B, respectively). The area enriched with F is sharply limited in the CB sample reacted in FW solution. In contrast, the SW CB sample showed a gradient with decreasing intensities towards the sample center.

Single isotope distribution maps showed that Na (Fig. 4C) and Mg (Fig. 4D) were quite homogeneously distributed in all samples and only slightly enriched in the RR. However, the Na isotope maps contrast with the EMPA results, which do not show any modifications in Na distribution, but this is most likely due to the lower sensitivity of EMPA (Fig. 3E). A mosaic image consisting of 16 single isotope maps from a SW sample revealed that Mg is not only enriched in the RR but also penetrated at least 300 µm deep into CB via the cortical canal network (CCN), which is reflected by a higher Mg content around the canaliculi. In contrast, the interstitial bone is less enriched with Mg (Fig. 4G). The altered CB samples were washed with MQ water several times before analysis to rinse out pore waters enriched with dissolved ions. It was impossible to distinguish between CCN and the interstitial CB material in the RR, because the interstitial bone was also enriched with Mg leading to a homogenous distribution within that area.

Calcium was found to be uniformly distributed in all samples. A slight increase in Ca was observed along the RR, the microcracks and porous structures (Fig. 4E). This observation again contrasts with the EMPA results (Fig. 3G). However, this can be explained by the nanoSIMS's lower sensitivity for Ca concentration. A significant depletion in P was observed within the RR (Fig. 4F), which correlates well with the EMPA results (Fig. 3F). In contrast, SW samples showed higher P contents along the margin and around larger pores (Fig. 4H). A distinct and uniform enrichment with Sr was determined along and exceeding the RR (Fig. 4J), irrespective of the type of solution. Further away from the edge of the samples, Sr was still detectable, but only directly surrounding the CCN and barely present in the interstitial bone. The same applies to Zn, although, to a lesser extent (Fig. 4I).

Most intriguingly, the elements Nd, Lu, and U (exclusively added to the aqueous solution of the FW experiments) were highly enriched along the edges of all FW samples, marking the RR. Mosaic images of Nd (Fig. 4K), Lu (Fig. 4L), and U (Fig. 4M), consisting of 30 individual nanoSIMS maps, revealed an increase of the penetration depth with increasing atomic number, i.e., 92 (U) > 71 (Lu) > 60 (Nd). However, the incorporation of U was thereby not restricted to the RR, i.e., U was transported further into the CB, comparable to Mg, Zn, and Sr, although the enrichment is less pronounced or detectable. In general, two different distribution patterns were observed: (1) a uniform change in element concentration in the RR, irrespective of histological features (Fig. 4A), and (2) some elements further penetrated deeper into the CB via the CCN. The latter is evident by higher element contents predominantly at the CB–solution–interface in cortical canals (Fig. 4J).

Representative isotope concentration profiles extracted from the nanoSIMS images of the FW series display the intensity of Sr, Nd, Lu, and U as a function of distance from the surface of the CB samples (Fig. 5). The greatly fluctuating Sr concentration profiles show that Sr deeply infiltrated the CB (Fig. 5A, B). In contrast, Nd, Lu, and U were only detected within the outermost 20 µm. In the 30 °C sample, Nd, Lu, and U showed relatively similar distribution patterns (Fig. 5A), whereas in the 60 °C sample a clearly distinct spatial distribution of these elements became apparent (Fig. 5B). The Nd content continuously decreased from the sample's edge towards the interior of the sample. However, Nd did

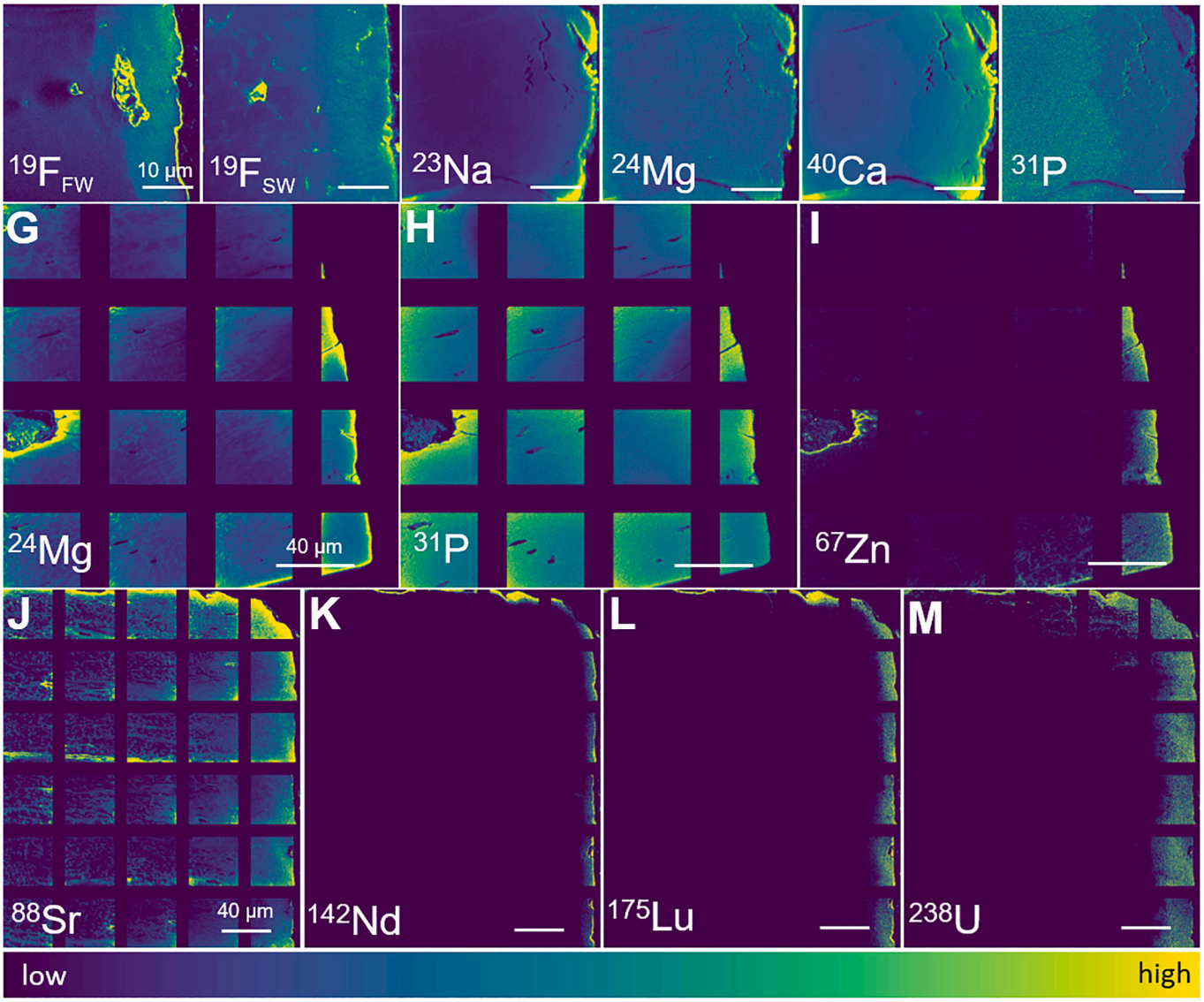

Fig. 4. Isotope distribution images obtained by nanoSIMS of representative cortical bone (CB) samples. (A) and (B) show the distribution of ^{19}F in an FW and an SW sample, respectively. Both samples reacted at 90 °C for 30 d. The CB sample exposed to FW for 30 d at 60 °C was chosen to show the distribution of (C) ^{23}Na, (D) ^{24}Mg, (E) ^{40}Ca, and (F) ^{31}P. The mosaic images, consisting of 16 and 30 individual maps, show the (G) ^{24}Mg, (H) ^{31}P, and (I) ^{63}Zn distribution and were taken from a sample that was reacted at 60 °C for 30 d in the SW solution. The last four mosaic images show the (J) ^{88}Sr, (K) ^{142}Nd, (L) ^{175}Lu, and (M) ^{238}U distribution in a representative CB sample reacted at 60 °C for 30 d in the FW experimental series (doped with REEs and U). The size of a single image is 40 × 40 µm^2.

not penetrate further into the CB than the outermost 10 µm. The shape of the U concentration curve can be described by relatively similar concentrations within the outermost 20 µm, limited by a sharp decline in concentration. The form of the Lu profile appears to be intermediate between the shape of the Nd and the U profile. The concentration profiles for the respective elements indicated a transition of the processes responsible for the uptake and incorporation of elements into CB. Concentration profiles of the equivalent 90 °C FW sample are missing because of the poor data quality of the nanoSIMS maps.

3.2.3. *Atomic-scale observations*

In the next step, APT measurements were performed to obtain information about the atomic-scale elemental and isotopic distribution within the RR. However, these measurements worked only to a limited extent and will not be further discussed. The results are included in Appendix 3.

3.3. *Phase composition and structural alteration of the bone apatite phase*

To characterize and quantify changes in the bone organic and mineral phase composition and structure of the bone apatite phase as a function of solution temperature at the micrometer scale, confocal Raman spectroscopic measurements were performed on a pristine CB sample and samples altered in SW and FW for 30 d at 30, 60, and 90 °C. Spectra were collected from the edge and the center of the samples. Fig. 6A shows representative Raman spectra in the wavenumber range between 900 and 1750 cm^{-1} from the outer bone rim of both 90 °C experiments along with a representative spectrum from the pristine bone.

These three spectra show the entire range of visible spectral variations in all 30 d samples. The spectra are characterized by an intense band near 960 cm^{-1} which can be assigned to the $v_1(PO_4)$ symmetrical stretching mode of the phosphate unit in the bone apatite, whose position is slightly shifted to higher wavenumbers in the RR of the experimentally altered samples (inset Fig. 6A). The Raman band at 1003 cm^{-1}

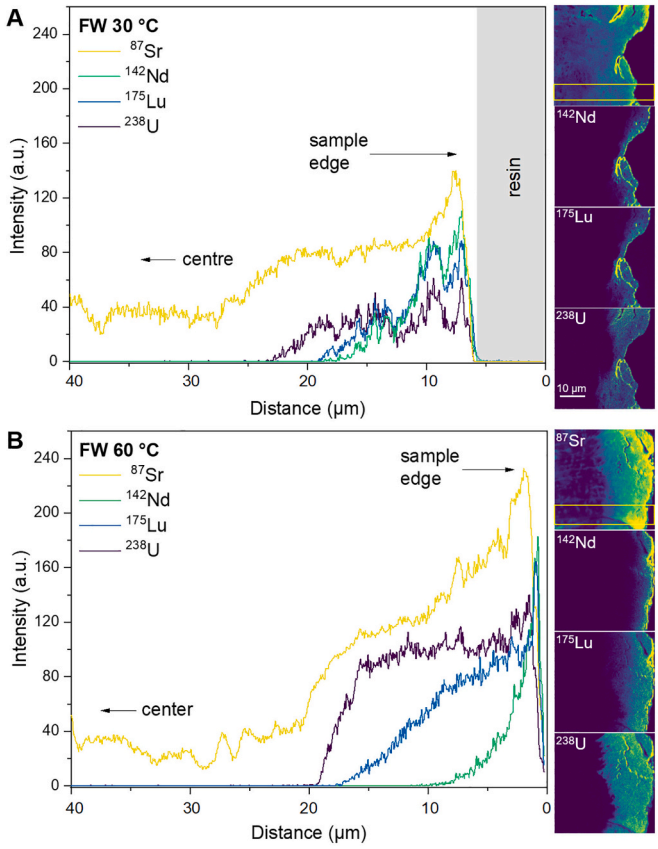

Fig. 5. NanoSIMS concentration profiles from FW samples. The intensity of ^{87}Sr, ^{142}Nd, ^{175}Lu, and ^{238}U nanoSIMS signals as a function of distance from the surface of CB samples immersed for 30 d in FW solution at (A) 30 °C and (B) 60 °C. The yellow boxes in the ^{87}Sr nanoSIMS maps mark the regions from which the concentration profiles were extracted/derived. a.u. = arbitrary units.

is assigned to the collagen constituent phenylalanine and is present in all spectra from altered samples. An additional, more intense band is visible near 1070 cm^{-1} that reflects the $v_1(CO_3)$ vibrational mode of the B-type carbonate group in the apatite lattice. This band partially overlaps with another phenylalanine band at 1033 cm^{-1} as well as with broad bands that can be attributed to the $v_3(PO_4)$ antisymmetric stretching vibrations of the phosphate group, complicating the quantification of the carbonate content from a Raman spectrum (Shah, 2020). The bands in the frequency range of 1215–1340 cm^{-1} and 1616–1720 cm^{-1} are related to vibrational modes of the collagen components amide III, comprising ν (C—N) and δ(N—H) vibrations, and amide I, respectively. Samples altered in SW resulted in spectra that can hardly be visibly differentiated from the spectra of the pristine CB sample. Only spectra from the RR formed at 90 °C show slightly less intense amide I and III bands, i.e., larger $v_1(PO_4)$-to-amide I/III intensity or mineral-to-collagen ratios. In contrast, Raman spectra from the RR of FW samples are characterized by strong photoluminescence (fluorescence) signals with two maxima at 866 and 872 nm, which can clearly be assigned to $^4F_{3/2} \rightarrow {}^4I_{9/2}$ electronic transitions in Nd^{3+}. This is further confirmed by a good spatial correlation between this photoluminescence signal and the relative Nd concentrations obtained by nanoSIMS (Fig. 6B, C).

To quantitatively evaluate the Raman data set, the $v_1(PO_4)$ band position is plotted against the normalized Nd photoluminescence signal (Fig. 7A). The overall strongest shift of the $v_1(PO_4)$ band to higher wavenumbers (frequencies) is observed in the FW 60 °C sample, although the important information here is that the Nd signal is not correlated with changes of the $v_1(PO_4)$ frequency.

Information about the structural state of the bone apatite is contained in the position and width of the $v_1(PO_4)$ band, the latter usually specified as FWHM. Both parameters were plotted against each other for all Raman data of each sample treated for 30 d in the SW (Fig. 7B) and FW solution (Fig. 7C). The band parameters obtained from the margin of the altered samples were compared with those obtained from the sample center and various pieces of the pristine bone. Along the edge of the SW samples, a significant shift $v_1(PO_4)$ band towards higher wavenumbers is observed at all three temperatures. There is a clear separation of the analyses from the sample margin compared to those from the pristine CB and the interior of the samples. The latter showed a clear shift towards lower FWHM but no shift to higher frequencies, i.e., in direction of the nano-crystalline HAp. Such a trend is also observed in the interior of FW samples, although even more pronounced. However, there is not such a distinct frequency difference between the analyses from the RR and the interior. Here, the $v_1(PO_4)$ frequency range is much higher and even spread than in SW samples. Surprisingly, the FWHM of the $v_1(PO_4)$ band did not change significantly but rather slightly increased when considering the entire data set. This is most pronounced for the 90 °C FW sample, where the FWHM values from the interior are significantly lower than those from the RR (Fig. 7C). In general, the position and width of the $v_1(PO_4)$ band of the less altered center of the FW and SW CB samples mark a linear trend towards well-ordered nano-crystalline HAp (Fig. 8; Asjadi et al., 2019). The frequency is comparable to those determined for pristine tooth dentin and modern lizard bone, but smaller than for pristine enamel (Fig. 8). Analyses from dentin experimentally altered in an initially F-free, acidic solution partly follow this trend (Weber et al., 2021).

3.4. Kinetics of element uptake by cortical bone

The solution composition after a given reaction time (Appendix 4) complements the chemical analyses of the altered bone samples. Overall, the concentrations of all elements, except P, show the strongest decrease already within the first three days. P was the only element initially released from the bone into the solution. In solutions derived from 60 or 90 °C experiments that ran for 14 d or longer, this was reversed and P was taken up from the solution into the bone. For B, the opposite was observed; after an initial distinct uptake into the bone within the first day, B was released back into the solution, slightly correlating with the increase in temperature.

The time-dependence of the Zn, Sr, Nd, Lu, and U contents in solution – elements predominantly enriched in the RR – can be used to gain quantitative insights into the kinetics of the overall trace element uptake process in CB. The element uptake is given by the difference between the concentration (mg/kg) of the element in the initial starting solution, c_i, and in the experimental solution after the experiments, c_a. For internal comparability, the element uptake was normalized by the specific tissue surface, σ, of each bone sample obtained by μCT (Kral et al., 2021). To scale the element uptake to the same surface area, a scaling factor B, given by $B = \sigma/\sigma_m$, was defined, where σ_m represents the average specific surface area from all CB samples. We then derive the following equation to compute the surface-normalized, percentage element uptake u_σ:

$$u_\sigma = B \bullet \frac{(c_i - c_a)}{c_i} \bullet 100 \quad (1)$$

In Fig. 9, the surface-normalized, percentage uptake of the elements Zn, Sr, Nd, Lu, and U from both solution types FW and SW were plotted as a function of time. From the graphs it becomes evident that the uptake rates slow down to zero already within the first three days, i.e., the element uptake reaches a saturation level. However, U is an exception in that it does not reach element uptake saturation in CB until after about 18 d (Fig. 9F). A two-parameter exponential function of the form

$$u_\sigma = S \bullet (1 - exp(-bt)) \quad (2)$$

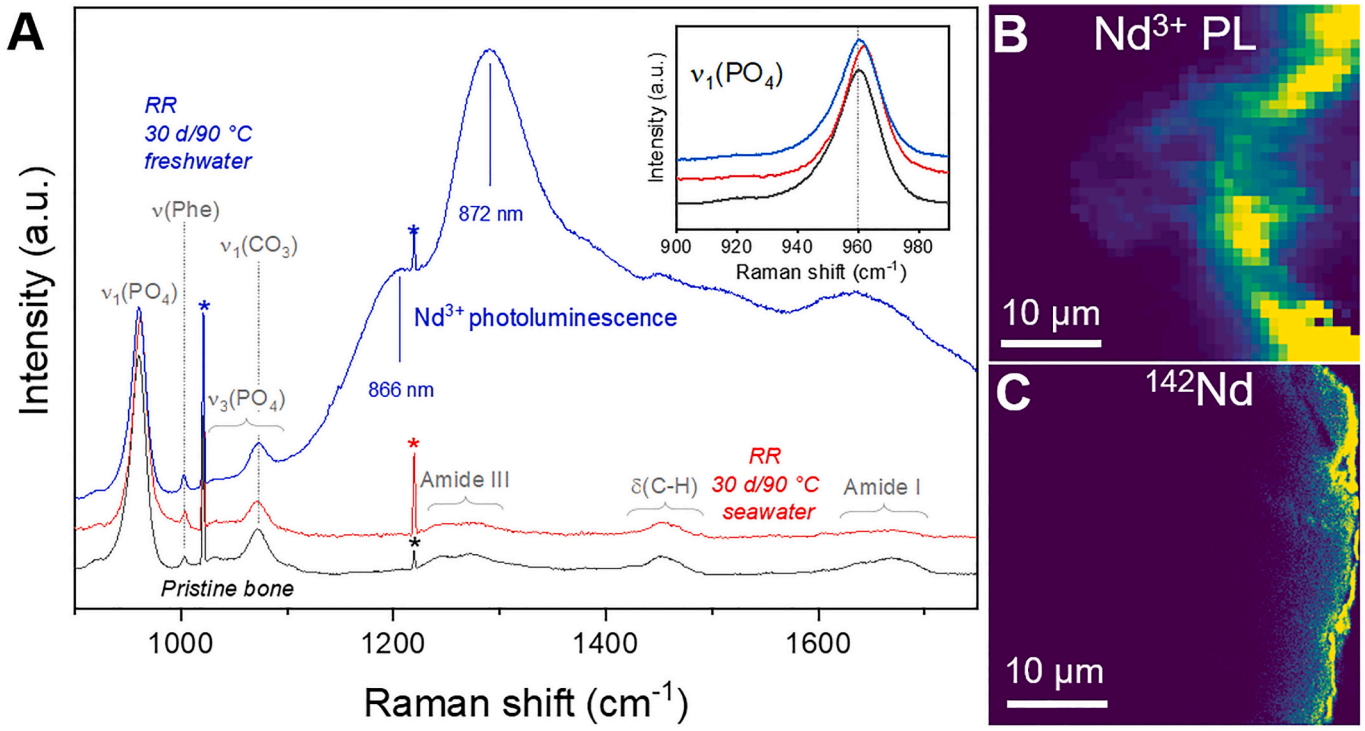

Fig. 6. Raman spectroscopic analysis of pristine cortical bone (CB) and the reaction rim (RR) of altered CB samples. (A) Raman spectra of pristine CB (black) as well as of representative CB samples altered in SW (red) and FW (blue) solutions for 30 d at 90 °C. Spectra were normalized to the maximum intensity of the $\nu_1(PO_4)$ band. The shift of this band is magnified for better comparison in the inset diagram in the upper right. (B) Hyperspectral Nd^{3+} photoluminescence image from a CB sample treated in FW solution for 30 days in comparison with (C) the corresponding nanoSIMS Nd distribution image. Differences between both images partly reflect surface changes due to re-polishing of the sample which was necessary to completely remove the nanoSIMS gold coating. (*) The sharp Raman bands are assigned to the laboratory room's ceiling light, which was used as an internal standard.

was found to be a suitable empirical function to fit the observed time evolution of u_σ and, thus, to determine the asymptotic saturation level, S, and the initial element uptake rates, r, for the elements Sr, Zn, U, Nd, and Lu from both solutions at each temperature (Appendix 5). The rate at a given time t is given by

$$r = \frac{du_\sigma}{dt} = S \bullet b \bullet exp(-bt) \quad (3)$$

and, thus, at $t = 0$, i.e., far from equilibrium by

$$r = S \bullet b \quad (4)$$

In Fig. 10A, the fit parameter S is given for the Zn, Sr, U, Lu, and Nd uptake from both solutions against temperature. The saturation level appears to increase linearly with temperature for all experiments, with Lu and Nd having the lowest positive slopes, both of which do not differ significantly from zero at the 95% confidence level, i.e., the saturation level of both RRs appears to have been independent of temperature.

From the rate r, it is possible to estimate the empirical activation energy, E_A, for the element uptake process(es). For this, ln(r) is plotted as a function of the inverse temperature in Fig. 10B (Arrhenius diagram). Suppose the activation energy of the process under consideration is constant over the investigated temperature interval, there should be a negative linear correlation with the slope, m, being proportional to the activation energy, i.e., $m = -E_A/R$ with R as the gas constant. Hence, the steeper the slope, the higher the activation energy. It is noticeable in Fig. 10B that, in general, there is only a very weak temperature dependency of the element uptake by CB. In fact, except for Nd, and Sr from SW, most of the slopes are positive if we fit a linear function to the data, which would imply unrealistic negative activation energies. However, the sampling number of the 30 °C experiments was smaller, so only the 1-day data points mainly control the fit parameter b in Eq. (2). This is particularly evident from the unrealistic fit of Eq. (2) to the U data from the 30 °C experiment (Fig. 9F), the results of which were also excluded from the plots in Fig. 10. Therefore, a linear equation was only fitted to the 60 and 90 °C data, excluding U as its uptake rates are significantly lower than those of the other elements. The slope yields empirical activation energy for the entire element uptake process of 13 ± 8 kJ/mol for the elements Zn, Sr, Nd, Lu, and U, which has a relatively large error but is different from zero with an error probability of 84%. Nevertheless, the 95% confidence and prediction intervals of the linear fit include most of the 30 °C data, but they do not include the U data, further indicating that the uptake of U is significantly slower than the uptake of the other elements. In addition, the activation energies were directly calculated from the slope of the tie lines between two data points of one experimental series, yielding a maximal value of ≈ 36 kJ/mol for Sr uptake in the SW solution. For U uptake, we obtain ≈ 9 kJ/mol, while the logarithm of the measured Zn uptake rate is positively correlated with $1/T$, suggesting a very low activation energy for Zn uptake.

3.5. Weight loss kinetics

The weight loss of the CB samples in the experiments with FW and SW solutions can be attributed predominantly to the decay and loss of collagen. While significantly less bioapatite was dissolved, the cortical porosity increased only marginally (Kral et al., 2021). Thus, the temperature-time dependency of the sample weight contains information about the kinetics of collagen decay. To account for different sizes of the CB samples, the measured weight loss was normalized to the initial specific volumes of the CB samples (Kral et al., 2021) and then plotted against the reaction time in Fig. 11. Since the weight loss is linearly correlated with time, an intercept-free linear-fitting model ($y = bx$) was used to determine the volume-normalized weight loss rate, w_L. In the FW experimental series (Fig. 11A), the rate was low at 30 and 60 °C, and not

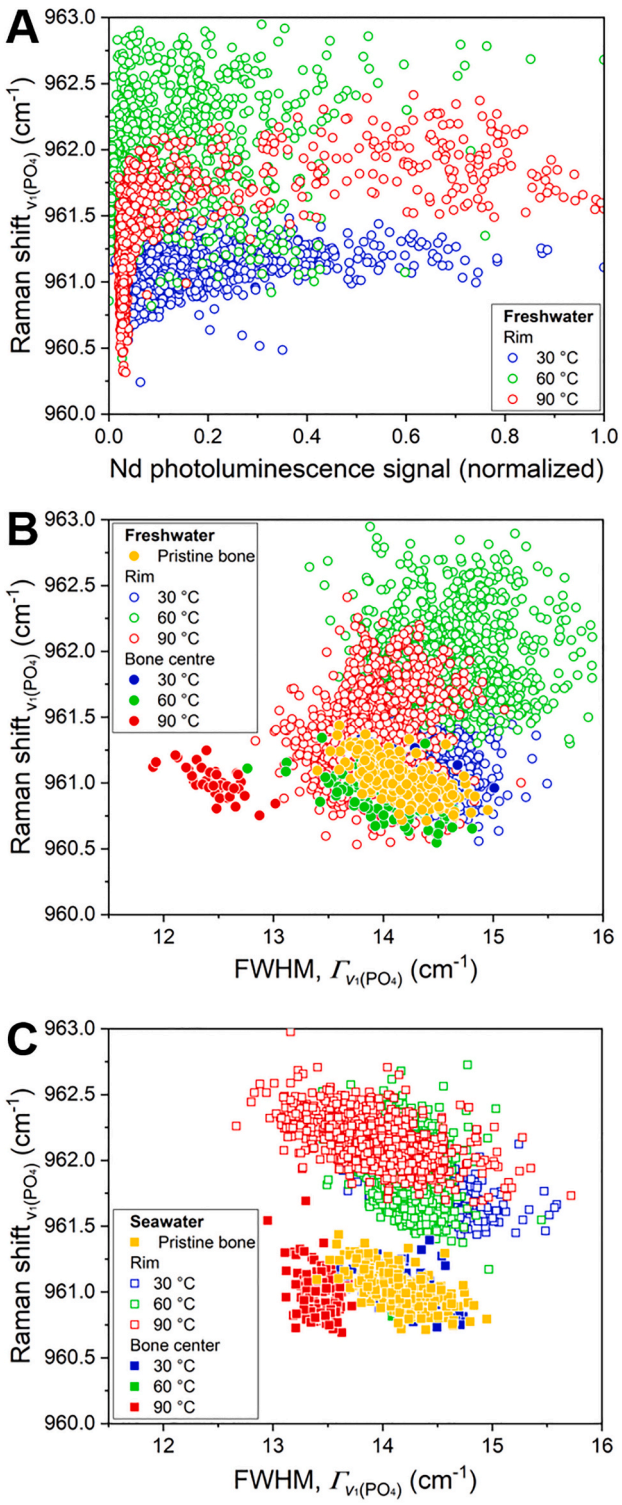

Fig. 7. Raman spectral parameters of pristine and altered cortical bone (CB) samples that were altered in SW and FW solutions. (A) The Raman shift of the $\nu_1(PO_4)$ band as a function of the normalized Nd photoluminescence signal for CB samples from all temperature regimes that were exposed to FW for 30 d at 30, 60, and 90 °C. (B) and (C) The frequency of the $\nu_1(PO_4)$ band as a function of its width given as full width at half maximum (FWHM) for pristine CB samples and CB samples that were reacted in SW and FW solution, respectively, for 30 d at 30 °C, 60 °C, and 90 °C in SW and FW solutions. Additionally, areas in the less altered sample center were measured for comparison due to the strong heterogeneity of the CB samples among each other.

significantly from zero ($w_L = 0.13 \pm 0.15 \bullet 10^{-6}$ mg/mm^{3}s and $5.3 \pm 3.4 \bullet 10^{-5}$ mg/mm^{3}s, respectively), but significantly higher at 90 °C ($w_L = 5.60 \pm 0.29 \bullet 10^{-4}$ mg/mm^{3}s). Nevertheless, if we plot the logarithms of the weight loss rates against $1/T$ in an Arrhenius diagram, we observe a linear relationship with a negative slope that corresponds to an empirical activation energy of $E_A = 61 \pm 11$ kJ/mol (Fig. 11C). In SW experiments, however, only the rate at 90 °C was significantly different from zero ($w_L = 1.26 \pm 0.22 \bullet 10^{-4}$ mg/mm^{3}s).

4. Discussion

4.1. Early structural and textural modifications of the cortical bone samples

BSE images of the altered CB samples clearly revealed that within just 1 d of the experiment, the formerly intact CB (Fig. 2A) had been strongly pervaded by microcracks (Fig. 2B-D). This contrasts with results from a previously conducted µCT study which showed that on a scale down to 3 µm the CB microarchitecture was largely unmodified (Kral et al., 2021). It is assumed that a voxel resolution of 3 µm could not resolve the majority of the small microcracks (Appendix 2). The CB samples immersed in FW solution for 1 day tended to show a temporal decrease in cortical porosity (e.g., $\Delta Ct.Po_{90\ °C,\ 1d,\ FW} = -15 \pm 3\%$; Kral et al., 2021). This could no longer be observed in the samples from the 3-day experiments, but the opposite (e.g., $\Delta Ct.Po_{90°C,\ 3d,\ FW} = 11 \pm 2\%$), while the number of microcracks did not change notably.

The question arises as to whether and how two opposing processes can occur simultaneously here: decrease in cortical porosity and the extensive formation of microcracks. In order to achieve a reduction in cortical porosity of about 15% by apatite precipitation, not only would the original porosity have to be reduced by 15%, but also the volume of the microcracks formed would have to be leveled out. It is very unlikely that this happened here, as there were simply not enough ions added to the solution, in particular P, to form this amount of apatite. Furthermore, this would have been reflected in an increase in weight rather than a slight decrease as observed (e.g. $\Delta wt_{90\ °C}$, 1d, FW $= -0.776 \pm 0.001\%$). Thus, it is assumed that collagen swelling (Koon, 2006), a temporary mechanism with large spatial impact (McKernan and Dailly, 1966), must have significantly reduced the cortical porosity after 1 d as hypothesized in Kral et al. (2021). The solution must therefore have penetrated large parts of the CCN only hours after the initiation of the experiment. This interpretation is indirectly supported by the deep infiltration of Sr, Mg, and Zn into the CB samples. Collagen swelling is caused by the interaction of collagen fibers with aqueous solutions, and its extent depends on the pH, temperature, and salinity of the aqueous solution. Collagen swelling can be suppressed by larger amounts of salt in an aqueous solution (Haines, 1987; Koon, 2006). This is probably the reason why such strong collagen swelling was not observed in SW samples (the salinity in SW solutions was 30 g/kg).

It is assumed that the microcracks were caused by air drying after the experiment was terminated. This is supported by the fact that the number of microcracks formed correlates negatively with the experimental duration and the collagen content of the CB samples (Kral et al., 2021). Even partially demineralized collagen shrinks during drying, which can lead to crack formation. Samples that have only been exposed to the solution for a short time have not yet degraded as much collagen as older samples, making them more susceptible to cracking. The older CB samples contain less collagen, which is also reflected in a high weight loss, especially for the 90 °C samples (Kral et al., 2021), and the bright areas on the BSE images clearly reflect a higher degree of mineralization. As a result, they are less susceptible to cracking during drying. It follows that the higher the temperature and the longer the experimental duration, the less cracking will occur.

Transferred to a natural environment, it is possible that bones exposed to multiple cycles of heating and cooling, as well as wetting and drying shortly after exposure to the environment, will experience

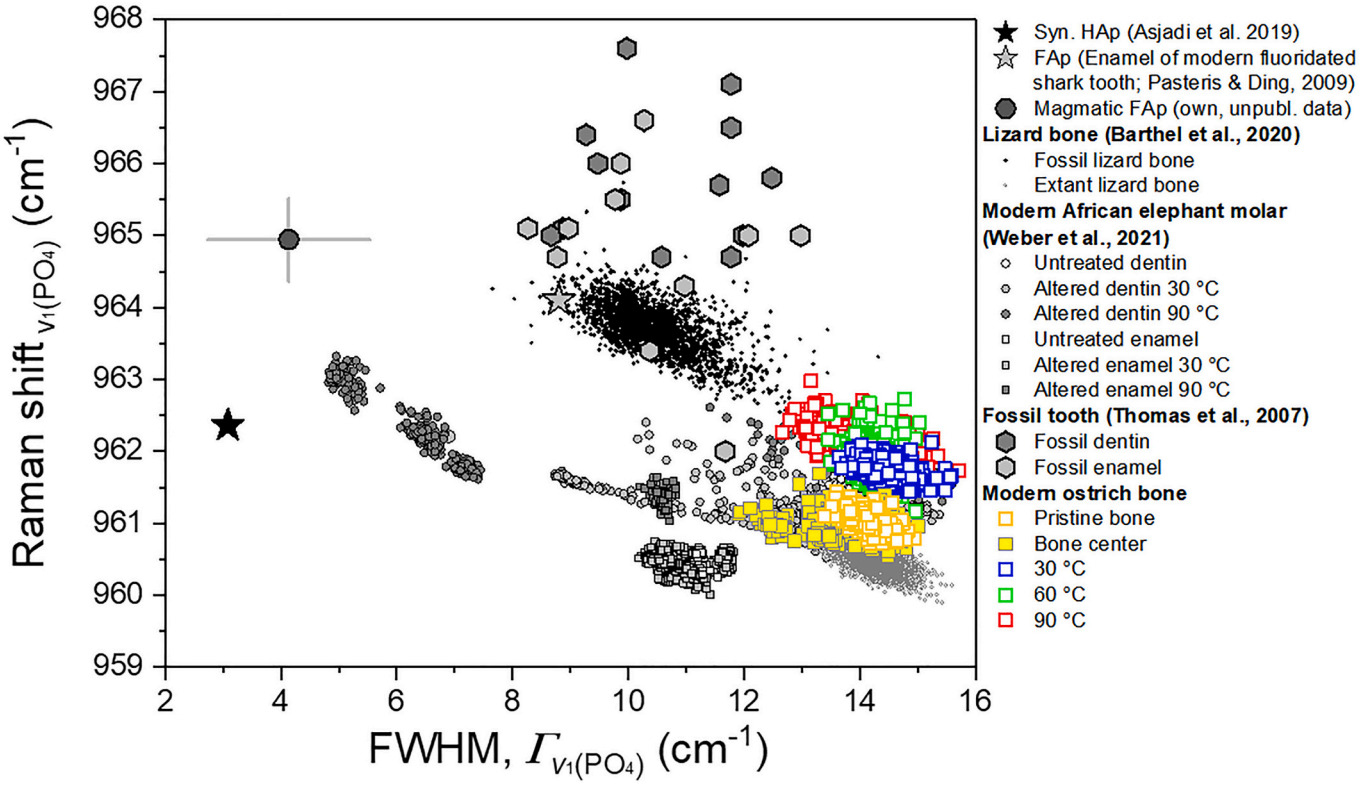

Fig. 8. Raman spectral parameters of reference materials and CB samples altered in a SW solution. The frequency of the $\nu_1(PO_4)$ band as a function of the band width, given as FWHM, for the SW experiment series in comparison with reference data from a pristine CB sample, different modern and fossil bones (Pasteris and Ding, 2009; Barthel et al., 2020) and teeth (Thomas et al., 2007), from experimentally altered teeth (Weber et al., 2021), synthetic HAp (Asjadi et al., 2019) and magmatic FAp (own, unpublished data).

greater mechanical weathering which can lead to rapid degradation of the bones. However, if the accessibility of bone to fluids is high, this can lead to the early formation of secondary minerals such as FAp. This in turn protects the bone from further degradation and contributes to its preservation (Conard et al., 2008; Thomas et al., 2012).

4.2. Element uptake and spatial distribution in cortical bone samples

Dissolved ions were transported via the aqueous solutions into the CB through the CCN and following collagen-crystallite interfaces. Directly along the sample's edge, an X-ray-dense, sharply delineated, up to 20 μm thick RR became visible in μCT (Kral et al., 2021) and BSE (Fig. 2F) images from samples altered in FW solutions. The RR was characterized by higher contents of Mg, Sr, Nd, Lu, and U. It is known that not only divalent molecules and cations (UO^{2+}, Sr^{2+}, and Zn^{2+}), but also mono-, tri-, tetra- and hexavalent cations (Na^{+}, REE^{3+}, U^{4+}, U^{6+}, respectively) can substitute for Ca^{2+} in a metastable HAp phase in compliance with a specific charge-compensating mechanism (Pan and Fleet, 2002; Trueman et al., 2004, 2006). CB samples derived from experiments with the SW solutions are characterized by an outer zone enriched with Sr and Zn, which is thus not visible in BSE and μCT images (Kral et al., 2021) but can also be considered a RR.

The penetration depth of the elements enriched in the RR also differed notably. The largest change in spatial distribution was observed for Mg, Zn, and Sr. These elements penetrated deepest into the CB sample and were highly enriched at the bone–solution–interface in the CCN. This demonstrates that the CCN was the preferred transport pathway, allowing for deep penetration of water and other dissolved chemical species to the interior of the bone. Another concurrent process is the diffusion of small molecules from the CCN into the osteocytes, which occurs within minutes at a temperature of 40 °C (Fernández-Seara et al., 2002). However, simple transport processes are assumed to prevail at least shortly after exposure of the samples to the solution. The CCN is anisotropically oriented with the majority of cortical canals running parallel to the bone surface (Fig. 1B). Cutting the samples from the bone perpendicular to its longitudinal growth direction the CCN made the cylindric bone samples more easily accessible for the solution even at a relatively low temperature. This is reflected by a thicker RR and greater intra-vascular penetration depth in the growth direction, i.e., along most cortical canals (Fig. 4K-M) - a pattern that corresponds well with the area enriched with Nd, Lu, and in particular with U (Fig. 3J-L). The penetration depth of these elements increased with increasing atomic number, i.e., 92 (U) > 71 (Lu) > 60 (Nd). Thus, these elements mark a relatively sharp concentration gradient towards the inside of the CB samples (Figs. 4K-M, 5), which agrees well with results from fossil bone (Herwartz et al., 2011). However, these concentration gradients must be associated with distinct reaction processes such as adsorption or crystallization rather than purely diffusional transport, as diffusivities of REEs and U in bone are too similar to cause such disparities (Kohn and Moses, 2012). The observed elemental fractionation within the RR possibly reflects different partition and adsorption coefficients (Hinz and Kohn, 2010; Trueman et al., 2011).

The RR was also depleted in Ca and P relative to the sample center, although the high greyscale values imply a higher density and/or a higher average atomic number than before the experiments. The relative depletion in P in the RR can be explained by the substitution of CO_3^{2-} for the PO_4^{3-} site in the apatite lattice, which is reflected by an increase in FWHM and by an intensity increase of $\nu_1(CO_3)$ relative to $\nu_1(PO_4)$ (Thomas et al., 2007).

Phosphorus was initially not contained in the experimental solutions, therefore a slight increase of P (<0.5 ppm) in the solutions had to be expected from apatite dissolution. However, in 60 and 90 °C experiments, after durations of 21 d, even these small amounts of P were again removed from the solutions most likely because the pore fluid became

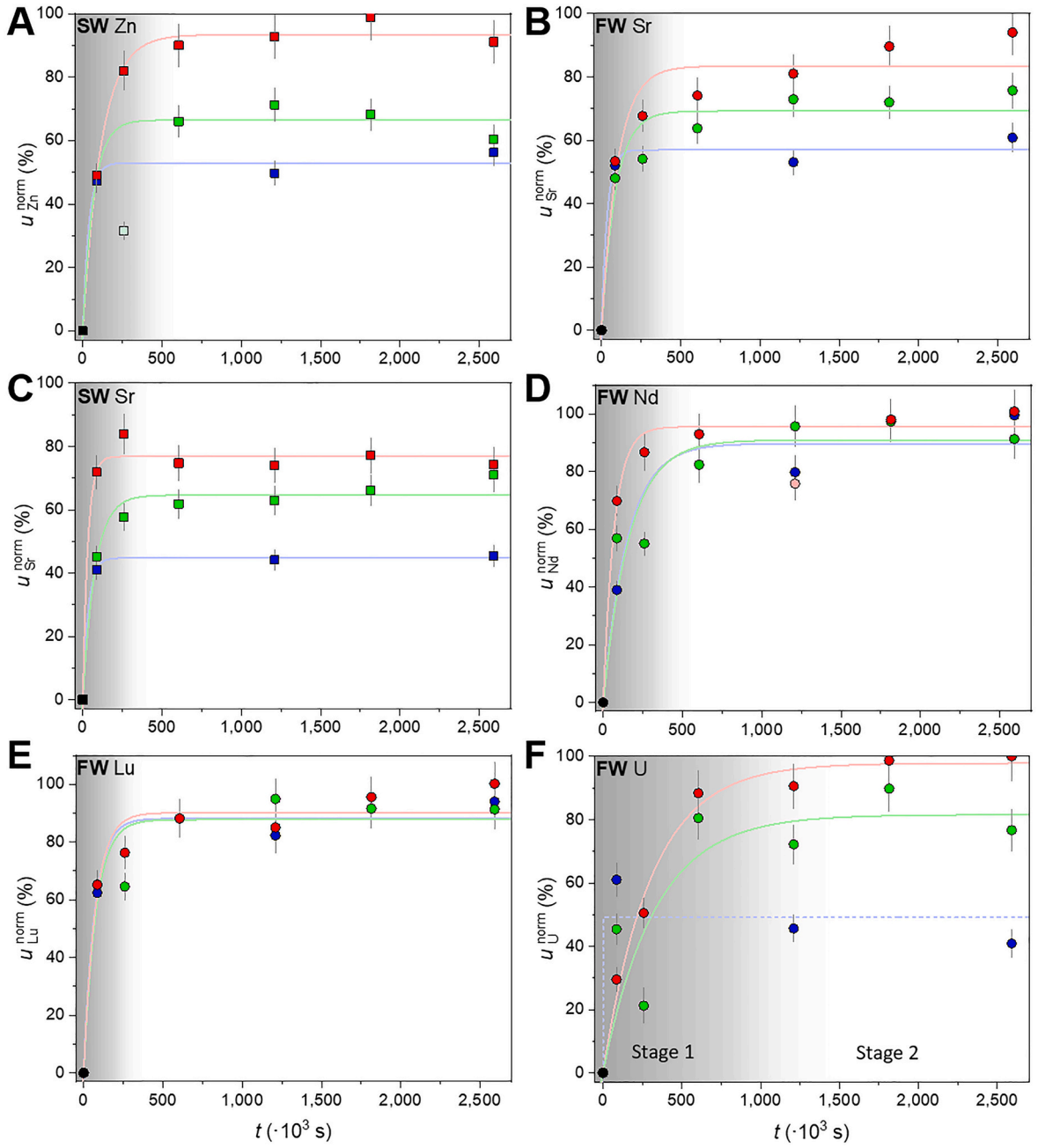

Fig. 9. Tissue surface-normalized element uptake from the solution into cortical bone. The diagrams A - F show the element uptake from SW or FW solutions as a function of time. (A) Zn from SW, (B) Sr from FW, (C) Sr from SW, (D - F) Nd, Lu, and U from FW, respectively. Error bars represent the 2-sigma error. Data points colored in blue, green, and red derive from 30, 60, and 90 °C experiments, respectively. Lightly colored data points in A and D were excluded as outliers from the fit.

saturated with HAp and apatite reprecipitation could take place. Such a mechanism has previously been suggested by Turner-Walker (2011). The decrease of P in the experimental solution indicates the formation of new apatite and/or the growth of pre-existing crystallites, reflected by a strong enrichment with Ca and P in the sample center (Fig. 3F, G). This presumably led locally to a higher degree of mineralization and here to a greater stability against cracking, fewer microcracks, and reduced micro-porosity over time (Turner-Walker, 2011; Kral et al., 2021). Raman spectra obtained from the sample center revealed a linear trend towards well-ordered nano-crystalline HAp (Asjadi et al., 2019), supporting this assumption. The trend is directly correlated with the increase in temperature (Figs. 7B, C and 8) and should result when both the size and the structural order of the nanometer-sized carbonated apatite crystallites increase by the recrystallization to carbonate-free HAp (De Mul et al., 1988; Shah, 2020) Note that in contrast to the RR, no F was incorporated in the center of the bone samples.

4.3. Bone apatite dissolution and/or recrystallization

The RR was visible on CT and BSE images after 1 d. However, this period is too short for assuming that a dissolution-recrystallization process has led to incorporating Nd, Lu, and U into the apatite lattice. It is more likely that they were first adsorbed onto the organic matrix and/or onto bioapatite crystallite surfaces. In the RR, strong photoluminescence signals (Fig. 6) related to $^4F_{3/2} \rightarrow {}^4I_{9/2}$ electronic transitions in Nd^{3+} were observed using Raman spectroscopy (Panczer et al., 2012; Lenz et al., 2013; Tuschel, 2016; Mikhalyova et al., 2019) with a laser excitation of 785 nm (Fau et al., 2022). It is common knowledge

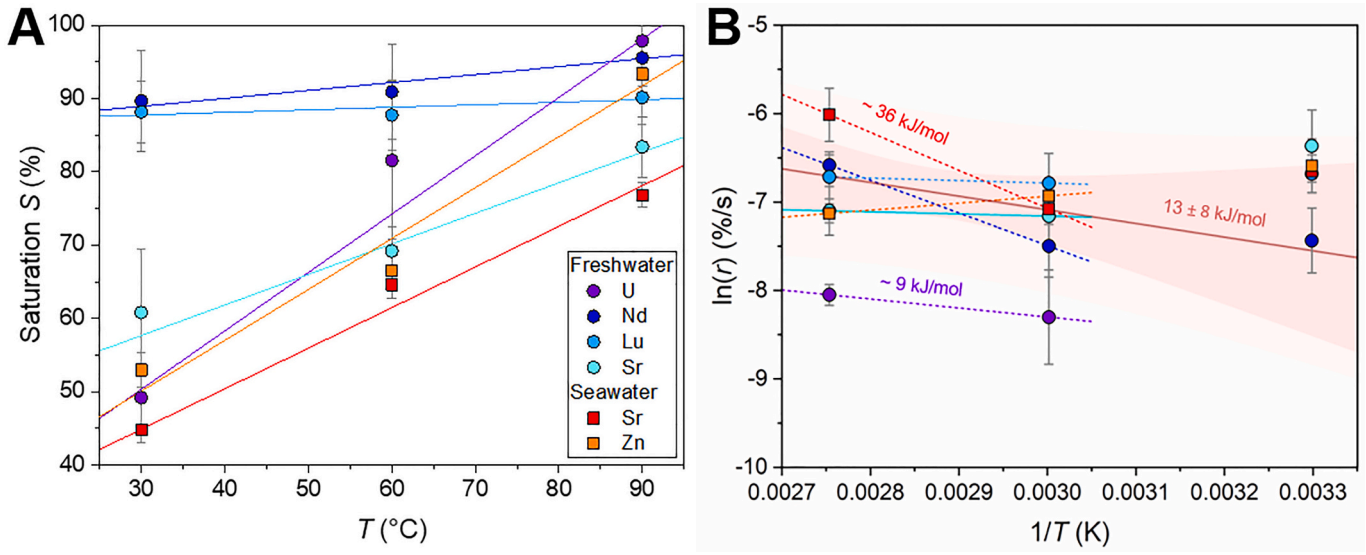

Fig. 10. Kinetics of element uptake. (A) Element saturation level, *S*, as a function of temperature for Sr, Nd, Lu, and U in FW experiments and Sr and Zn in SW experiments. (B) The logarithm of the element uptake rate, *r*, is plotted against the inverse temperature. The symbol legend applies to both plots.

that REEs act as the main luminescence centers in minerals (Amoroso and Pope, 2015). Thus, in the case of the formation of secondary apatite (with incorporated Nd or Lu), the occurrence and intensity of the photoluminescence signal are expected to correlate with a blue shift of the $v_1(PO_4)$ band, which would indicate a shortening of the average P—O bond length and thus the formation of a less defect or F-rich apatite phase. However, such a correlation was not observed (Fig. 7A). Moreover, the photoluminescence signal was already detectable after 1 d in the 30 °C temperature regime, while the $v_1(PO_4)$ band was not significantly shifted during the entire experimental duration. Consequently, it is more likely that Nd, which is used as a contrasting agent in electron microscopy, because it concentrates in tissues (Koeppenkastrop and De Carlo, 1992; Koehler et al., 2005; Kuipers and Giepmans, 2020), is adsorbed onto the organic matrix and/or onto the surface of the nanocrystalline bone apatite crystallites instead of being incorporated into newly grown or recrystallized apatite. To a certain extent, the same applies to U, which has also high biosorption properties (Volesky and Holan, 1995), wherefore $[UO_2]^{2+}$ di-cations can bind to negatively charged amino acid residues in collagen (Tzaphlidou et al., 1982). Furthermore, in an experiment conducted by Kohn and Moses (2012), it was demonstrated that U concentration was about 60 times higher in collagen-bearing than in deproteinated bone. The interaction between collagen and the dissolved ions might also have been supported by the initially occurring collagen swelling, whereby the collagen surface was drastically enlarged, providing more options for adsorption and temporally impeding the penetration into CB. Furthermore, this interpretation is also supported by the observed low activation energy for elemental uptake of about 13 kJ/mol.

Over time and accelerated by heat the organic matrix was continuously hydrolyzed, which is reflected by a distinct weight loss of up to 20%, especially in 60 and 90 °C experiments (Fig. 11; Kral et al., 2021). Collagen degradation led to the exposure of the bone HAp crystallite surfaces to the solution so that dissolution and/or recrystallization of the nm-sized bone apatite crystals was accelerated. In addition, hydrolysis and/or denaturation of collagen releases amorphous calcium phosphate into the pore solution, which is located in the gap regions of collagen and acts as a bioapatite nucleation inhibitor (Nudelman et al., 2010; Lotsari et al., 2018). Higher Na contents detected in those areas enriched with Nd and Lu may indicate apatite recrystallization, as the replacement of Ca^{2+} by REE^{3+} requires a monovalent charge-balancing ion like Na^+ (Voigt et al., 2017), but generally, charge compensation may also be achieved by defect-formation, resulting in non-stoichiometric, Ca-deficit HAp (Asjadi et al., 2019).

Notably, solution analyses revealed (after an initial uptake) a release of B from the CB sample into the solution over time, particularly in 90 °C experiments. Boron is known to strengthen bone by binding either to the hydroxyl group of HAp and/or collagen I (Rondanelli et al., 2020 and references therein). Thus, the release of B into solution can imply both intensified dissolution of the apatite phase and degradation of collagen - which occurred first cannot be clearly determined.

The observed linear relationship between the weight-loss rates (w_L) in FW experiments and the inverse temperature yielded an empirical activation energy E_A of 61 ± 11 kJ/mol. Information on collagen degradation kinetics under wet conditions is scarce. Nevertheless, this value can be compared with an E_A determined for the decay of bone collagen in hydrochloric acid which varies between 6.8 and 25.1 kJ/mol (Castro-Ceseña et al., 2011), while the denaturation of bone collagen induced by heat and under dry conditions (T = 450–670 K) requires an activation energy of 127 ± 8 kJ/mol (Lambri et al., 2016). It is recalled that in both experimental series, w_L was accelerated by increasing the temperature from 60 to 90 °C (Fig. 8A, B). These results basically fit with observations made in a thermal study on unmineralized and mineralized collagen, which showed that in a hydrated environment the internal cross-links between collagen fibrils break at 65 ± 5 °C and denaturation starts, ultimately leading to collagen degradation at more elevated temperatures (Bozec and Odlyha, 2011) and thus to weight loss. The distinctly lower weight loss rates in SW experiments clearly showed the effect of the (local) pH on the kinetics of bone apatite recrystallization, particularly concerning the recrystallization window (pH range between 7.6 and 8.1) defined by Berna et al. (2004) under which apatite recrystallization was enhanced. Thus, it is conceivable that higher recrystallization rates - reflected by an increase in greyscale intensity in the sample's interior - in SW experiments counterbalanced the heat-induced collagen loss, which would also fit with the observed lower number of microcracks. Raman spectra of FW samples did not allow conclusions to be drawn concerning collagen degradation or preservation due to intense photoluminescence signals covering the collagen-related Raman bands. In the SW sample, however, a significant reduction of the intensity of collagen-related Raman bands, e.g., the amide I or III bands, was observed, which is clear evidence for collagen degradation (Fig. 5A).

Raman spectra obtained from the RR showed a shift of the $v_1(PO_4)$ band position to higher frequencies in both experimental series. The shift is related to a shortening of the P—O bond length in the phosphate

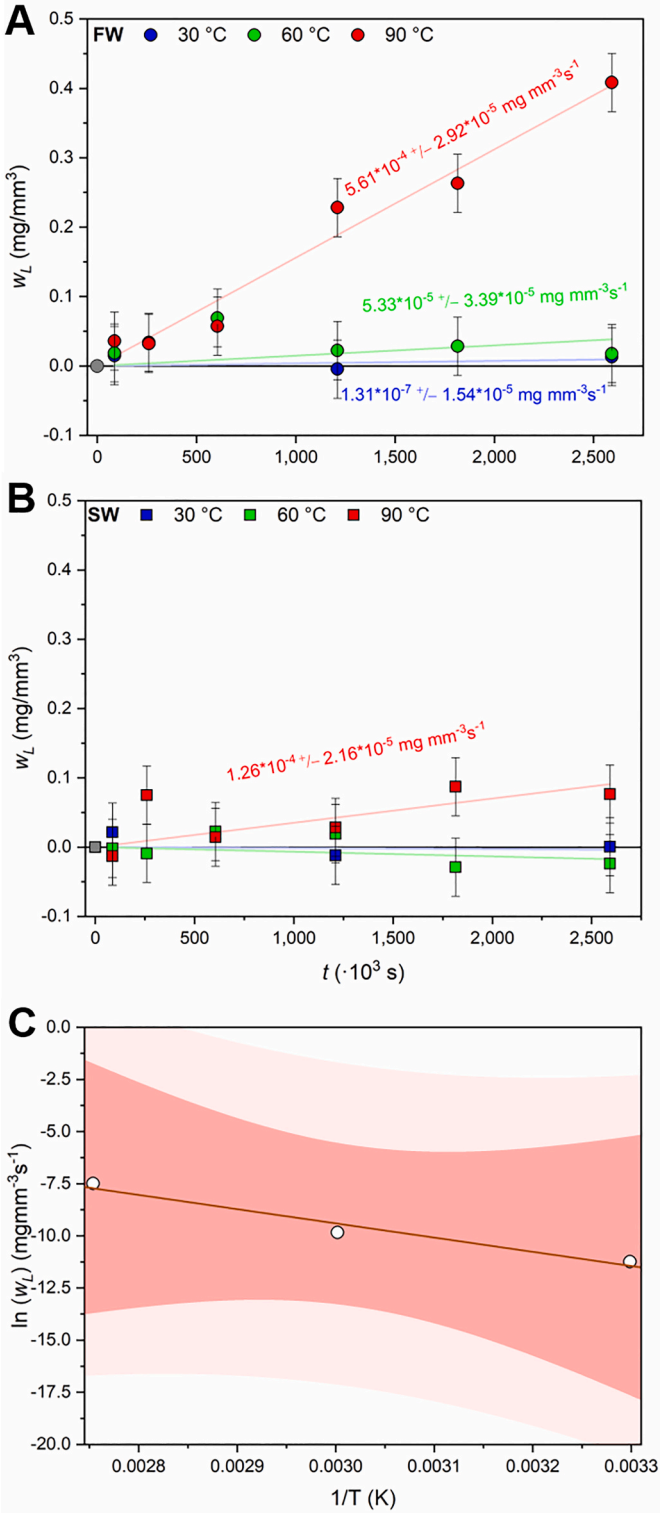

Fig. 11. Weight loss kinetics. Volume-normalized weight loss (w_L) as a function of time. Weight loss rates were calculated for samples exposed to (A) FW and (B) SW solutions for each temperature. (C) w_L rates were plotted in an Arrhenius diagram against the inverse temperature.

tetrahedra of the apatite lattice, likely due to the incorporation of F^- in the OH^- position. The presence of F was also shown by nanoSIMS element maps, with a distinct enrichment in F within the RR. However, this contrasts with the increase of the FWHM, which, based on the physics of crystal vibrations, is expected to decrease, in particular, when FAp is formed. This unusual positive shift in the frequency versus the width diagram may be explained by the convolution of the $v_1(PO_4)$ band of two structurally slightly different nano-crystalline apatite phases, as, for instance, of FAp and HAp crystallites, forming one broader band with a maximum that is shifted to a higher frequency. In any case, these results provide evidence for the dissolution of bioapatite nano-crystals followed by the formation of an F-bearing phase, e.g., authigenic carbonated-FAp, in the RR, and a nano-crystalline, well-ordered, i.e., carbonate-poor, HAp-phase in the sample's interior. Overall, they suggest that two different processes take place simultaneously but independently from each other. On the one hand, the Raman data from the RR indicate that the carbonated bioapatite crystallites are partly replaced by carbonated FAp, likely by an interface-coupled dissolution-reprecipitation mechanism that has been proposed as the dominant mechanism in mineral replacement processes (Ruiz-Agudo et al., 2014; Putnis, 2021). This process is thermodynamically driven by the difference in the solubility of the parent and product apatite. However, in the center part of the CB samples, were F is absent, the situation is different. Here, it is conceivable that the bioapatite was partly replaced by carbonate-poor or -free HAp (Turner-Walker, 2011) through an interface-coupled dissolution-reprecipitation process, especially at high temperatures. In this case, the carbonated bioapatite has a higher aqueous solubility than a carbonate-free or -poor HAp, which in turn has a higher solubility than FAp (Zhu et al., 2009; Qiao et al., 2017). It follows that the latter will form if F is available (Aufort et al., 2019). We recall that both replacement processes produce a distinct trend in the relationship between the frequency and width of the $v_1(PO_4)$ band (Fig. 8).

4.4. Element uptake mechanisms and kinetics

3D reconstructions of μCT data showed that the RR is unevenly distributed around each CB sample (Kral et al., 2021). Consequently, the bone microstructure has a large impact on the local element uptake and thus on spatial element distribution. It is assumed, that the element's concentration, the physicochemical milieu in the aqueous solution, the element's partition and adsorption coefficients, the speciation of the element, and the porosity/permeability of the bone are the parameters predominantly controlling element uptake (Trueman and Tuross, 2002). In general, the term 'element uptake' into bone covers both the penetration of solutions carrying dissolved ions into the CB as well as the incorporation of elements into the apatite lattice either due to adsorption processes, dissolution-reprecipitation by a ripening process, or due to an interface-coupled dissolution-reprecipitation process (Putnis, 2009). The results of the present study clearly show that it is crucial to separately consider element uptake and incorporation, considering them as the result of different, parallel, and/or consecutive transport and reaction processes.

4.4.1. Element uptake

It is known that because of its spongy properties, bone tends to soak up aqueous solutions carrying various elements within short time scales (Trueman and Tuross, 2002). The element distribution and BSE images did not reveal any significant modifications after 1 d, although 40 to 70 wt% of the initial element concentration in solution, except P, were already removed from the solution within 1 d. Element uptake saturation levels were reached after 7 d (Fig. 7), with increasing saturation level from 30 to 90 °C (Fig. 8A). However, distinct microstructural changes became first observable after exposure of CB to the experimental solution for >14 d. Thus, it is conceivable that an initially fast transport process led to an instantaneous pervasion of the bone by the solution and element adsorption to collagen and/or the bone apatite nano-crystals until the bone was saturated in solution. During this quick process, double-charged ions, such as Mg, Sr, or Zn were transported in solution following interfaces and cracks deep into the bone (Fig. 4G, I, J, respectively), while tri- or higher valent elements such as Nd, Lu, and U

were solely concentrated along the outer bone rim. In aqueous solutions, the predominant species of Nd, Lu, and U are Nd^{3+} (Panigrahi et al., 2016), a fully hydrated Lu^{3+} species ($[Lu(OH_2)_8]^{3+}$ (Rudolph and Irmer, 2018), and uranyl di-cations $[UO_2]^{2+}$, respectively. The high absorption coefficients for the dissolved Nd^{3+} and Lu^{3+} ions between water and apatite surfaces (Koeppenkastrop and De Carlo, 1992) as well as their tendency to form complexes with organics (Kuipers and Giepmans, 2020) probably lead to a rapid removal from the pore fluids (Trueman et al., 2004) shortly after entering the CCN (see section 4.3.). Thus, these elements were rapidly scavenged from the ambient aqueous solution into the RR, while divalent cations were able to penetrate deeper into the CB via the CCN carried by the solution.

4.4.2. Element incorporation

Element distribution patterns in the bone reflect transport and reaction processes, such as recrystallization of the bone apatite phase, and/or adsorption on crystallite surface sites (Millard and Hedges, 1996; Kohn, 2008). Although the exact underlying mechanisms are still not fully understood, it is widely assumed that element distribution within and incorporation into bone mainly occur via different transport mechanisms and not via volume diffusion (Millard and Hedges, 1996; Kohn, 2008; Herwartz et al., 2011; Kohn and Moses, 2012) leading to strong differences in the distribution of, e.g., REE in bones on a µm-scale (Suarez et al., 2010). However, the data gathered in the present study clearly revealed that the element distributions differ even on a sub-µm-scale.

The most prominent diffusion models to explain the element/isotope incorporation into bone are (1) diffusion plus adsorption (DA) of trace elements onto crystallite surface sites, leading to a continuously decreasing concentration gradient towards the interior of fossil bone (Millard and Hedges, 1996); (2) diffusion plus reaction or recrystallization (DR) as a result of bioapatite nanocrystalline surfaces being exposed to a fluid and thus initiating surface-driven dissolution-recrystallization processes, which finally leads to the formation of secondary apatite crystals of different compositions. A sharp border between altered, i.e., recrystallized material and unaltered material is characteristic for DR (Kohn, 2008); (3) the double-medium diffusion model (DMD), which describes the occurrence of two diffusion pathways with different transport properties. DMD concentration profiles typically show very steep concentration gradients in the outermost part of the bone, similar to DA profiles. Concentrations are also decreasing with distance, but not as much as in DA models. Characteristic for this type of diffusion model is the still relatively high trace element concentration quite far away from the bone's surface, which is assumed to be related to fast, inter-crystalline diffusion (Kohn, 2008).

In a study performed by Suarez and Kohn (2020) REE and U concentration profiles of partially and completely fossilized bone samples obtained by LA-ICPMS were assigned to different diffusion models. They postulated that the exponentially decreasing concentration profile of REEs is typical for either DA or DMD, while the U profile is associated with DR. These results do not entirely match with the observations made in our study. The here observed concentration plots of nanoSIMS isotope distribution images can be better explained by a transition from an initially transport-controlled process (^{142}Nd) towards a transport-reaction process, whereby the reactive part became the predominant part with increasing atomic number ($^{175}Lu \rightarrow {}^{238}U$). The intensity profile of Lu can be best described as an intermediate state between DA and DR. It should be noted that the enrichment of Nd, Lu, and U in the RR is presumably not due to lower concentrations in the pore water but rather to rapid adsorption and subsequent incorporation by local interface-coupled dissolution-reprecipitation. The solution data in Fig. 9 show that saturation occurred relatively quickly, but even after 30 d, small amounts of Nd and Lu were still present in the solution. In Trueman et al. (2011), the adsorption coefficients for the different REEs were determined: that for Nd is significantly higher than that for Lu, which is consistent with our observations.

The concentration profile of Sr shows a different pattern which is similar to a DMD profile. However, it is suggested that instead of fast, inter-crystalline diffusion, a simple transport-reaction process must have caused the higher Sr concentrations further away from the sample's edge - the same applies for Mg and Zn. One possible process is a fast, kinetically uninhibited transport of elements by the solution that percolated through isolated pathways, i.e. the CCN. This is followed by adsorption and/or local interface-coupled dissolution-reprecipitation reactions, which are much slower. NanoSIMS images showed unambiguously that the respective elements were only concentrated around the CCN, whereas diffusion in nano-crystalline bioapatite would have led to an even enrichment in the interstitial bone (Fig. 4G, I-M).

Here, it needs to be mentioned that with quantitative point analysis or line scans, isotope distributions on such a small scale cannot be resolved, in particular not by using µm-sized spot sizes, because every single measurement would cover much more unaltered than altered bone areas. NanoSIMS analysis, however, provides an extremely high lateral resolution of 50–150 nm and high mass resolution, thereby allowing to determine any element and its isotopes at the nanometer scale and resolve such element distribution patterns. However, the resolution is still by far not good enough to resolve intra-nanocrystalline chemical patterns.

4.4.3. Reaction kinetics

The time-dependent chemical data revealed that the element uptake of Zn, Sr, Nd, Lu, and U into bone was only barely kinetically inhibited and that the uptake occurred rapidly after the CB samples were exposed to the aqueous solutions - for all elements except U, a saturation level was reached already within the first three days. A clear positive linear relationship between the height of the saturation level in CB samples and the temperature was found for Zn, Sr, and U, while the uptake of Nd and Lu seems to have been independent of temperature (Fig. 9). Fernández-Seara et al. (2002) have investigated diffusional transport mechanisms of water in CB using NMR imaging and spectroscopy. Their experiments at different temperatures revealed a distinct temperature-dependency for the diffusional transport of water through the CB matrix. It was further found that the interaction between water and the bone matrix is diffusion-limited, which is reflected by a higher activation energy of E_A = 26.8 kJ/mol than for self-diffusion of free liquid bulk water (E_A = 18.9 kJ/mol; Mills, 1973; Fripiat et al., 1984). The activation energies determined in the present study of about 13 kJ/mol (Appendix 5) are in the order of that for self-diffusion of water, i.e., the element uptake into bone was not significantly kinetically inhibited.

5. Conclusions

The *in vitro* alteration experiments and analytical techniques were designed, respectively applied to identify the distinct transport and reaction processes during the interaction of cortical bone with different aqueous solutions under simulated early diagenetic conditions. The most prominent finding is that distinct modifications of the major and trace element composition in bone caused by post mortem alteration processes started immediately after the bone's exposure to artificial freshwater and seawater-like solutions. The element uptake rates slowed down to almost zero within the first three but not later than after 18 d. The second major finding is that significant alteration of both the organic and mineral phase, particularly at the margins of the bone samples, occurred already within the first few hours to days after exposure to an aqueous solution and not after several years as previously assumed. Most elements, particularly Sr, Nd, Lu, and U were concentrated behind a diffusion/transport-reaction front near the sample's surface, which is only clearly detectable in samples exposed to freshwater solutions. Concentration profiles covering the reaction rim revealed a transition from an initially transport-controlled process (^{142}Nd) towards a transport-reaction process (^{175}Lu), whereby the reactive part is more dominant the larger the atomic number (^{238}U) is.

Additionally, fast transport-reaction processes led to the rapid distribution and enrichment of Ca, Mg, Sr, and Zn within the cortical bone through the infiltration of the solution along the cortical canals.

From these results a more detailed, albeit phenomenological model for the interaction between cortical bone, aqueous solutions, and the elements dissolved therein can be derived: it is here suggested that the elements concentrated in the reaction rim are first and immediately bound by adsorption onto collagen fibrils and/or onto crystallite surfaces. Then, collagen hydrolysis, accelerated by heat, leads to the release of these elements, dissolved amorphous calcium phosphate, and bioapatite components into the pore fluid. The surface of the bioapatite is exposed to the pore fluid, which promotes its dissolution, and the precipitation and recrystallization of apatite are facilitated. The dissolved apatite constituents Ca and P were relocated into the sample's interior forming carbonate-poor, nano-crystalline, well-ordered hydroxylapatite while thermodynamically more stable, authigenic, and F-bearing apatite crystals were likely formed in the reaction rim. Early recrystallization and formation of more stable carbonated fluorapatite might protect the bone against further alteration and could slow down the uptake of external elements during later stages of diagenesis. Furthermore, within a few weeks, also carbonate-poor or -free hydroxylapatite is recrystallized in the sample center independent of the processes occurring in the reaction rim. Moreover, it is important to point out that, Sr and Mg, both proxies for paleo-reconstructions, are altered and were incorporated from the aqueous solutions that penetrate much deeper into large areas of the bone samples within quite short time periods. The results further demonstrate that the surrounding aqueous environment present immediately *post mortem*, e.g. rainwater puddle, lake, river, or ocean, has a major impact on the preservation or degradation of bone and thus on the degree of early diagenetic chemical and mineralogical modifications.

Human rights

This article does not contain any studies with human subjects performed by any of the authors.

Animal studies

This article does not contain any studies with animal subjects performed by any of the authors.

Declaration of Competing Interest

The authors declare that they have no conflict of interest.

Data availability

Data will be made available on request.

Acknowledgments

We would like to thank Denis Fougerouse, David Saxey, William Rickard, and Steven Reddy from the Geoscience Atom Probe for preparing and analyzing the atom probe cones as well as Alexander Ziegler for valuable comments on earlier versions of the manuscript. Funding for this study was provided by the Deutsche Forschungsgemeinschaft (DFG), grant nos. GE 1094/23-1 and TU 148/9-1. This is contribution nos. 43 of the DFG Research Unit 2685 "The Limits of the Fossil Record: Analytical and Experimental Approaches to Fossilization" and contribution no. 68 of the LA-ICPMS laboratory of the Institut für Geowissenschaften, Universität Bonn. The manuscript was significantly improved by comments from Gordon Turner-Walker and one anonymous reviewer.

Appendix A. Supplementary data

Supplementary data to this article can be found online at https://doi.org/10.1016/j.chemgeo.2022.121060.

References

Abdel-Maksoud, G., 2010. Comparison between the properties of 'accelerated-aged' bones and archaeological bones. Mediterr. Archaeo. Ar. 10, 89–112.
Amoroso, A.J., Pope, S.J.A., 2015. Using lanthanide ions in molecular bioimaging. Chem. Soc. Rev. 44, 4723–4742. https://doi.org/10.1039/C4CS00293H.
Asjadi, F., Geisler, T., Salahi, I., Euler, H., Mobasherpour, I., 2019. Ti-substituted hydroxylapatite precipitated in the presence of titanium sulfate: a novel photocatalyst? Am. J. Chem. Appl. 6, 1–10.
Aufort, J., Gervais, C., Ségalen, L., Labourdette, N., Coelho-Diogo, C., Baptiste, B., Beyssac, O., Amiot, R., Lécuyer, C., Balan, E., 2019. Atomic scale transformation of bone in controlled aqueous alteration experiments. Palaeogeogr. Palaeoclimatol. Palaeoecol. 526, 80–95. https://doi.org/10.1016/j.palaeo.2019.03.042.
Barthel, J.H., Fougerouse, D., Geisler, T., Rust, J., 2020. Fluoridation of a lizard bone embedded in Dominican amber suggests open-system behavior. PLoS One 15 (2), e0228843. https://doi.org/10.1371/journal.pone.0228843.
Beard, B.L., Johnson, C.M., 2000. Strontium isotope composition of skeletal material can determine the birth place and geographic mobility of humans and animals. J. Forensic Sci. 45, 1049–1061.
Berna, F., Matthews, A., Weiner, S., 2004. Solubilities of bone mineral from archaeological sites: the recrystallization window. J. Archaeol. Sci. 31, 867–882. https://doi.org/10.1016/j.jas.2003.12.003.
Boskey, A.L., Robey, P.G., 2013. The regulatory role of matrix proteins in mineralization of bone in osteoporosis. In: Marcus, R., Feldman, D., Dempster, D.W., Luckey, M., Cauley, J.A. (Eds.), Osteoporosis. Academic Press, Cambridge, pp. 235–255. https://doi.org/10.1016/B978-0-12-415853-5.00011-X.
Bourgon, N., Jaouen, K., Bacon, A.-M., Jochum, K.P., Dufour, E., Duringer, P., Ponche, J.-L., Joannes-Boyau, R., Boesch, Q., Antoine, P.-O., Hullot, M., Weis, U., Schulz-Kornas, E., Trost, M., Fiorillo, D., Demeter, F., Patole-Edoumba, E., Shackelford, L.L., Dunn, T.E., Zachwieja, A., Duangthongchit, S., Sayavonkhamdy, T., Sichanthongtip, P., Sihanam, D., Souksavatdy, V., Hublin, J.-J., Tütken, T., 2020. Zinc isotopes in late Pleistocene fossil teeth from a Southeast Asian cave setting preserve paleodietary information. PNAS 117, 4675–4681. https://doi.org/10.1073/pnas.1911744117.
Bozec, L., Odlyha, M., 2011. Thermal denaturation studies of collagen by microthermal analysis and atomic force microscopy. Biophys. J. 101, 228–236. https://doi.org/10.1016/j.bpj.2011.04.033.
Castro-Ceseña, A.B., Noviskaya, E.E., Chen, P.-Y., Hirate, G.A., McKittrick, J., 2011. Kinetic studies of bone demineralization at different HCl concentrations and temperatures. Mater. Sci. Eng. C 31, 523–530. https://doi.org/10.1016/j.msec.2010.11.003.
Collins, M.J., Nielsen-Marsh, C.M., Hiller, J., Smith, C.I., Roberts, J.P., Prigodich, R.V., Wess, T.J., Csapò, J., Millard, A.R., Turner-Walker, G., 2002. The survival of organic matter in bone: a review. Archaeometry 44, 383–394.
Conard, N.J., Walker, S.J., Kandel, A.W., 2008. How heating and cooling and wetting and drying can destroy dense faunal elements and lead to differential preservation. Palaeogeogr. Palaeoclimatol. Palaeoecol. 266, 236–245. https://doi.org/10.1016/j.palaeo.2008.03.036.
Davis, M., Pineda-Munoz, S., 2016. The temporal scale of diet and dietary proxies. Ecol. Evol. 6, 1883–1897. https://doi.org/10.1002/ece3.2054.
De Mul, F.F.M., Otto, C., Greve, J., Arends, J., Ten Bosch, J.J., 1988. Calculation of the Raman line broadening on carbonation in synthetic hydroxyapatite. J. Raman Spectrosc. 19, 13–21. https://doi.org/10.1002/jrs.1250190104.
DeNiro, M.J., 1985. Postmortem preservation and alteration of in vivo bone collagen isotope ratios in relation to palaeodietary reconstruction. Nature 317, 806–809.
DeNiro, M.J., Epstein, S., 1978. Influence of diet on the distribution of carbon isotopes in animals. Geochim. Cosmochim. Acta 42, 495–506.
DeNiro, M.J., Epstein, S., 1981. Influence of diet on the distribution of nitrogen isotopes in animals. Geochim. Cosmochim. Acta 45, 341–351.
Dobberstein, R.C., Collins, M.J., Craig, O.E., Taylor, G., Penkmann, K.E.H., Ritz-Timme, S., 2009. Archaeological collagen: why worry about collagen diagenesis? Archaeol. Anthropol. Sci. 1, 31–42. https://doi.org/10.1007/s12520-009-0002-7.
Donovan, J.J., Hanchar, J.M., Picolli, P.M., Schrier, M.D., Boatner, L.A., Jarosewich, E., 2003. A re-examination of the rare-earth-element orthophosphate standards in use for electron-microprobe analysis. Can. Mineral. 41, 221–232. https://doi.org/10.2113/gscanmin.41.1.221.
Ericson, J.E., 1985. Strontium isotope characterization in the study of prehistoric human ecology. J. Hum. Evol. 14, 503–514.
Fau, A., Beyssac, O., Gauthier, M., Panczer, G., Gasnault, O., Meslin, P.Y., Bernard, S., Maurice, S., Boulliard, J.C., Bosc, F., Drouet, C., 2022. Time-resolved Raman and luminescence spectroscopy of synthetic REE-doped hydroxylapatites and natural apatites. Am. Mineral. https://doi.org/10.2138/am-2022-8006.
Fernández-Seara, M.A., Wehrli, S.L., Wehrli, F.W., 2002. Diffusion of exchangeable water in cortical bone studied by nuclear magnetic resonance. Biophys. J. 82, 522–529. https://doi.org/10.1016/S0006-3495(02)75417-9.
Fogel, M.L., Tuross, N., 2003. Extending the limits of paleodietary studies of humans with compound specific carbon isotope analysis of amino acids. J. Archaeol. Sci. 30, 535–545. https://doi.org/10.1016/S0305-4403(02)00199-1.

Fricke, H.C., Rogers, R.R., Backlund, R., Dwyer, C.N., Echt, S., 2008. Preservation of primary stable isotope signals in dinosaur remains, and environmental gradients of the late cretaceous of Montana and Alberta. Palaeogeogr. Palaeoclimatol. Palaeoecol. 266, 13–27. https://doi.org/10.1016/j.palaeo.2008.03.030.

Fripiat, J.J., Letellier, M., Levitz, P., 1984. Interaction of water with clay surfaces. Philos. Trans. R. Soc. Lond. 311, 287–299. https://doi.org/10.1098/rsta.1984.0029.

Geisler, T., Menneken, T., 2021. Raman spectroscopy in fossilization research: Basic principles, applications in paleontology, and a case study on an acanthodian fish spine. In: Gee, C.T., McCoy, V.E., Sander, P.M. (Eds.), Fossilization: Understanding the Material Nature of Ancient Plants and Animals. John Hopkins University Press, Baltimore, pp. 73–114.

Glimcher, M.J., 2006. Bone: nature of the calcium phosphate crystals and cellular, structural, and physical chemical mechanisms in their formation. Rev. Mineral. Geochem. 64, 223–282. https://doi.org/10.2138/rmg.2006.64.8.

Goldstein, J.I., Newbury, D.E., Echlin, P., Joy, D.C., Romig Jr., A.D., Lyman, C.E., Fiori, C., Lifshin, E., 1992. Quantitative X-ray analysis: the basics. In: Goldstein, J.I., Newbury, D.E., Echlin, P., Joy, A.C., Romig Jr., A.D., Lyman, C.E., Fiori, C., Lifshin, E. (Eds.), Scanning Electron Microscopy and X-Ray Microanalysis. Springer, Boston, MA, pp. 395–416. https://doi.org/10.1007/978-1-4613-0491-3_8.

Grandfield, K., Vuong, V., Schwarcz, H.P., 2018. Ultrastructure of bone: hierarchical features from nanometer to micrometer scale revealed in focused ion beam sections in the TEM. Calcif. Tissue Int. 103, 606–616. https://doi.org/10.1007/s00223-018-0454-9.

Guiry, E., Royle, T.C.A., Matson, R.G., Ward, H., Weir, T., Waber, N., Brown, T.J., Hunt, B.P.V., Price, M.H.H., Finney, B.P., Kaeriyama, M., Qin, Y., Yang, D.Y., Szpak, P., 2020. Differentiating salmonid migratory ecotypes through stable isotope analysis of collagen: archaeological and ecological applications. PLoS One 15, e0232180. https://doi.org/10.1371/journal.pone.0232180.

Haines, B.M., 1987. Shrinkage temperature in collagen fibres. Leather Conserv. News 3, 1–5.

Hedges, R.E.M., 2002. Bone diagenesis: an overview of processes. Archaeometry 44, 319–328. https://doi.org/10.1111/1475-4754.00064.

Hedges, R.E.M., Stevens, R.E., Richards, M.P., 2004. Bone as a stable isotope archive for local climatic information. Quat. Sci. Rev. 23, 959–965. https://doi.org/10.1016/j.quascirev.2003.06.022.

Henderson, P., Marlow, C.A., Molleson, T.I., Williams, C.T., 1983. Patterns of chemical change during bone fossilization. Nature 306, 358–360.

Herwartz, D., Tütken, T., Münker, C., Jochum, K.P., Stoll, B., Sander, P.M., 2011. Timescales and mechanisms of REE and Hf uptake in fossil bones. Geochim. Cosmochim. Acta 75, 82–105. https://doi.org/10.1016/j.gca.2010.09.036.

Herwartz, D., Tütken, T., Jochum, K.P., Sander, P.M., 2013. Rare-earth element systematics of fossil bone revealed by LA-ICPMS analysis. Geochim. Cosmochim. Acta 103, 161–183. https://doi.org/10.1016/j.gca.2012.10.038.

Heuser, A., Tütken, T., Gussone, N., Galer, S.J.G., 2011. Calcium isotopes in fossil bones and teeth — diagenetic versus biogenic origin. Geochim. Cosmochim. Acta 75, 3419–3433. https://doi.org/10.1016/j.gca.2011.03.032.

Hinz, E.A., Kohn, M.J., 2010. The effect of tissue structure and soil chemistry on trace element uptake in fossils. Geochim. Cosmochim. Acta 74, 3213–3231. https://doi.org/10.1016/j.gca.2010.03.011.

Hoppe, K.A., Koch, P.L., Carlson, R.W., Webb, S.D., 1999. Tracking mammoths and mastodons: reconstruction of migratory behavior using strontium isotope ratios. Geology 27, 439–442. https://doi.org/10.1130/0091-7613(1999)027<0439:TMAMRO>2.3.CO;2.

Jans, M.M.E., 2008. Microbial bioerosion of bone-a review. In: Wisshak, M., Tapanila, L. (Eds.), Current Developments in Bioerosion: Erlangen Earth Conference Series. Springer-Verlag, Berlin, pp. 397–413.

Jaouen, K., Pons, M.-L., Balter, V., 2013. Iron, copper and zinc isotopic fractionation up mammal trophic chains. Earth Planet. Sci. Lett. 374, 164–172.

Jarosewich, E., Boatner, L.A., 1991. Rare-earth element reference samples for electron microprobe analysis. Geostand. Geoanal. Res. 15, 397–399. https://doi.org/10.1111/j.1751-908X.1991.tb00115.x.

Jarosewich, E., White, J.S., 1987. Strontianite reference sample for electron microprobe and SEM analyses. J. Sediment. Res. 57, 762–763. https://doi.org/10.1306/212F8C10-2B24-11D7-8648000102C1865D.

Jarosewich, E., Nelen, J.A., Norberg, J.A., 1980. Reference samples for electron microprobe analysis. Geostand. Newslett. 4, 43–47. https://doi.org/10.1111/j.1751-908X.1980.tb00273.x.

Karr, L.P., Outram, A.K., 2012. Bone degradation and environment: understanding, assessing and conducting archaeological experiments using modern animal bones. Int. J. Osteoarchaeol. 25, 201–212. https://doi.org/10.1002/oa.2275.

Kasioptas, A., Geisler, T., Putnis, C.V., Perdikouria, C., Putnis, A., 2010. Crystal growth of apatite by replacement of an aragonite precursor. J. Cryst. Growth 312 (16–17), 2431–2440. https://doi.org/10.1016/j.jcrysgro.2010.05.014.

Keenan, S.W., Engel, A., 2017. Early diagenesis and recrystallization of bone. Geochim. Cosmochim. Acta 196, 209–223. https://doi.org/10.1016/j.gca.2016.09.033.

Koehler, S.J., Harouiya, N., Chaïat, C., Oelkers, E.H., 2005. Experimental studies of REE fractionation during water–mineral interactions: REE release rates during apatite dissolution from pH 2.8 to 9.2. Chem. Geol. 222, 168–182. https://doi.org/10.1016/j.chemgeo.2005.07.011.

Koeppenkastrop, D., De Carlo, E.H., 1992. Sorption of rare-earth elements from seawater onto synthetic mineral particles: an experimental approach. Chem. Geol. 95, 251–263. https://doi.org/10.1016/0009-2541(92)90015-W.

Kohn, M.J., 2008. Models of diffusion-limited uptake of trace elements in fossils and rates of fossilization. Geochim. Cosmochim. Acta 72, 3758–3770. https://doi.org/10.1016/j.gca.2008.05.045.

Kohn, M.J., Moses, R.J.M., 2012. Trace element diffusivities in bone rule out simple diffusive uptake during fossilization but explain in vivo uptake and release. PNAS 110, 419–424. https://doi.org/10.1073/pnas.1209513110.

Kohn, M.J., Schoeninger, M.J., Barker, W.W., 1999. Altered states. Effects of diagenesis on fossil tooth chemistry. Geochim. Cosmochim. Acta 63, 2737–2747. https://doi.org/10.1016/S0016-7037(99)00208-2.

Kolodny, Y., Luz, B., Sander, P.M., Clemens, W.A., 1996. Dinosaur bones: Fossils or pseudomorphs? The pitfalls of physiology reconstruction from apatite fossils. Palaeogeogr. Palaeoclimatol. Palaeoecol. 126, 161–171. https://doi.org/10.1016/S0031-0182(96)00112-5.

Koon, H.E.C., 2006. Detecting Cooked Bone in the Archaeological Record: A Study of the Thermal Stability and Deterioration of Bone Collagen. Ph.D. thesis. University of York (243 pp).

Kowalik, N., Anczkiewicz, R., Wilczyński, J., Wojtal, P., Müller, W., Bondioli, L., Nava, A., Gasparik, M., 2020. Tracing human mobility in Central Europe during the Upper Paleolithic using sub-seasonally resolved Sr isotope records in ornaments. Sci. Rep. UK 10, 10386. https://doi.org/10.1038/s41598-020-67017-2.

Kral, A.G., Ziegler, A., Tütken, T., Geisler, T., 2021. Experimental aqueous alteration of cortical bone microarchitecture analyzed by quantitative micro-computed tomography. Front. Earth Sci. 9, 609496 https://doi.org/10.3389/feart.2021.609496.

Kronick, P.L., Cooke, P., 1996. Thermal stabilization of collagen fibers by calcification. Connect. Tissue Res. 33, 275–282. https://doi.org/10.3109/03008209609028885.

Kuipers, J., Giepmans, B.N.G., 2020. Neodymium as an alternative contrast for uranium in electron microscopy. Histochem. Cell Biol. 153, 271–277. https://doi.org/10.1007/s00418-020-01846-0.

Lambri, M.L., Giordano, E.D., Bozzano, P.B., Bonifacich, F.G., Pérez-Landazábal, J.I., Zelada, G.I., Gargicevich, D., Recarte, V., Lambri, O.A., 2016. Thermal degradation of type I collagen from bones. J. Renew. Mater. 4, 251–257. https://doi.org/10.7569/JRM.2016.634111.

Lenz, C., Talla, D., Ruschel, K., Skoda, R., Götze, J., Nasdala, L., 2013. Factors affecting the Nd^{3+} (REE^{3+}) luminescence of minerals. Mineral. Petrol. 107, 415–428. https://doi.org/10.1007/s00710-013-0286-2.

Levin, N.E., Cerling, T.E., Passey, B.H., Harris, J.M., Ehleringer, J.R., 2006. A stable isotope aridity index for terrestrial environments. PNAS 103, 11201–11205. https://doi.org/10.1073/pnas.0604719103.

Longinelli, A., 1984. Oxygen isotopes in mammal bone phosphate: a new tool for palaeoclimatological and palaeoenvironmental research? Geochim. Cosmochim. Acta 48, 385–390.

Lotsari, A., Rajasekharan, A.K., Halvarsson, M., Andersson, M., 2018. Transformation of amorphous calcium phosphate to bone-like apatite. Nat. Commun. 9, 4170. https://doi.org/10.1038/s41467-018-06570-x.

Martin, J.E., Tacail, T., Balter, V., 2017. Non-traditional isotope perspectives in vertebrate palaeobiology. Paleontology 60, 485–502. https://doi.org/10.1111/pala.12300.

Matthiesen, H., Høier Eriksen, A.M., Hollesen, J., Collins, M., 2021. Bone degradation at five Arctic archaeological sites: quantifying the importance of burial environment and bone characteristics. J. Archaeol. Sci. 125, 105296 https://doi.org/10.1016/j.jas.2020.105296.

McKernan, W.M., Dailly, S.D., 1966. The relationship between swelling of hard tissue collagen in acid and alkali and the presence of phosphate cross-links. In: Fleisch, H., Blackwood, H.J.J., Owen, M. (Eds.), Calcified Tissues. Springer, Berlin, Heidelberg, pp. 171–174. https://doi.org/10.1007/978-3-642-49802-2_33.

Mikhalyova, E.A., Khomenko, O.V., Gavrilenko, K.S., Dotsenko, V.P., Addison, A.W., Pavlishchuk, V.V., 2019. Absorption- and excitation-modulated luminescence of Pr^{3+}, Nd^{3+}, and Lu^{3+} compounds with dianions of tetrafluoroterephthalic and camphoric acids. ACS Omega 4, 2669–2675. https://doi.org/10.1021/acsomega.8b02388.

Millard, A.R., Hedges, R.E.M., 1996. A diffusion-adsorption model of uranium uptake by archaeological bone. Geochim. Cosmochim. Acta 60, 2139–2152. https://doi.org/10.1016/0016-7037(96)00050-6.

Mills, R., 1973. Self-diffusion in normal and heavy water in the range 1-45.deg. J. Phys. Chem. 77, 685–688. https://doi.org/10.1021/j100624a025.

Monti, F., Robert, A., Dominici, J.M., Sforzi, A., Bagur, R.T., Navarro, A.M., Guillou, G., Duriez, O., Bentaleb, I., 2021. Using GPS tracking and stable multi-isotopes for estimating habitat use and winter range in Palearctic ospreys. Oecologia 195, 655–666. https://doi.org/10.1007/s00442-021-04855-5.

Nielsen-Marsh, C.M., Hedges, R.E.M., 2000. Patterns of diagenesis in bone I: the effects of site environments. J. Archaeol. Sci. 27, 1139–1150. https://doi.org/10.1006/jasc.1999.0537.

Nudelman, F., Pieterse, K., George, A., Bomans, P.H.H., Friedrich, H., et al., 2010. The role of collagen in bone apatite formation in the presence of hydroxyapatite nucleation inhibitors. Nat. Mater. 9, 1004–1009. https://doi.org/10.1038/nmat2875.

Pan, Y., Fleet, M.E., 2002. Compositions of the apatite-group minerals: Substitution mechanisms and controlling factors. Rev. Mineral. Geochem. 48, 13–49. https://doi.org/10.2138/rmg.2002.48.2.

Panczer, G., Ligny de, D., Mendoza, C., Gaft, M., Seydoux-Guillaume, A.-M., Wang, X., 2012. Raman and fluorescence. In: Dubessy, J., Caumon, M.-C., Rull, F. (Eds.), Raman Spectroscopy Applied to Earth Sciences and Cultural Heritage, European Mineralogical Union Notes in Mineralogy, vol. 12, pp. 61–82. https://doi.org/10.1180/EMU-notes.12.2.

Panigrahi, M., Grabda, M., Kozak, D., Dorai, A., Shibata, E., Kawamura, J., Nakamura, T., 2016. Liquid-liquid extraction of neodymium ions from aqueous solutions of $NdCl_3$ by phosphonium-based ionic liquids. Sep. Purif. Technol. 171, 263–269. https://doi.org/10.1016/j.seppur.2016.07.044.

Pasteris, J.D., Ding, D.Y., 2009. Experimental fluoridation of nanocrystalline apatite. Am. Mineral. 94, 53–63. https://doi.org/10.2138/am.2009.2926.
Pasteris, J.D., Yoder, C.H., Wopenka, B., 2014. Molecular water in nominally unhydrated carbonated hydroxylapatite: the key to a better understanding of bone mineral. Am. Mineral. 99, 16–27. https://doi.org/10.2138/am.2014.4627.
Philibert, J., Tixier, R., 1968. Electron penetration and the atomic number correction in electron probe microanalysis. J. Phys. D. Appl. Phys. 1, 685–694. https://doi.org/10.1088/0022-3727/1/6/302.
Pucéat, E., Reynard, B., Lécuyer, C., 2004. Can crystallinity be used to determine the degree of chemical alteration of biogenic apatites? Chem. Geol. 205, 83–97. https://doi.org/10.1016/j.chemgeo.2003.12.014.
Putnis, A., 2002. Mineral replacement reactions: from macroscopic observations to microscopic mechanisms. Mineral. Mag. 66 (5), 689–708. https://doi.org/10.1180/0026461026650056.
Putnis, A., 2009. Mineral replacement reactions. Rev. Mineral. Geochem. 70, 87–124. https://doi.org/10.2138/rmg.2009.70.3.
Putnis, A., 2021. Fluid–mineral interactions: controlling coupled mechanisms of reaction, mass transfer and deformation. J. Petrol. 62egab092 https://doi.org/10.1093/petrology/egab092.
Qiao, W., Liu, Q., Li, Z., Zhang, H., Chen, Z., 2017. Changes in physicochemical and biological properties of porcine bone derived hydroxyapatite induced by the incorporation of fluoride. Sci. Technol. Adv. Mater. 18, 110–121. https://doi.org/10.1080/14686996.2016.1263140.
Reddy, S.M., Saxey, D., Rickard, W., Fougerouse, D., Montalvo, S.D., Verberne, R., Riessen, A., 2020. Atom probe tomography: development and application to the geosciences. Geostand. Geoanal. Res. 44, 5–50. https://doi.org/10.1111/ggr.12313.
Reynard, B., Balter, V., 2014. Trace elements and their isotopes in bones and teeth: diet, environments, diagenesis, and dating of archeological and paleontological samples. Palaeogeogr. Palaeoclimatol. Palaeoecol. 416, 4–16. https://doi.org/10.1016/j.palaeo.2014.07.038.
Reznikov, N., Bilton, M., Lari, L., Stevens, M.M., Kröger, R., 2018. Fractal-like hierarchical organization of bone begins at the nanoscale. Science 360. https://doi.org/10.1126/science.aao2189 eaao2189.
Rickard, W., Reddy, S.M., Saxey, D., Fougerouse, D., Timms, N., Daly, L., Peterman, E.M., Cavosie, A.J., Jourdan, F., 2020. Novel applications of FIB-SEM-based ToF-SIMS in atom probe tomography workflows. Microsc. Microanal. 26, 1–8. https://doi.org/10.1017/S1431927620000136.
Rondanelli, M., Faliva, M.A., Peroni, G., Infantino, V., Gasparri, C., Iannello, G., Perna, S., Riva, A., Petrangolini, G., Tartara, A., 2020. Pivotal role of boron supplementation on bone health: a narrative review. J. Trace Elem. Med. Biol. 62, 126577 https://doi.org/10.1016/j.jtemb.2020.126577.
Rudolph, W., Irmer, G., 2018. Hydration and ion pair formation in aqueous Lu^{3+}-solution. Molecules 23, 3237. https://doi.org/10.3390/molecules23123237.
Ruiz-Agudo, E., Putnis, C.V., Putnis, A., 2014. Coupled dissolution and precipitation at mineral–fluid interfaces. Chem. Geol. 383, 132–146. https://doi.org/10.1016/j.chemgeo.2014.06.007.
Saloman, E.B., Craig, J.S., 2006. Wavelengths, energy level classifications, and energy levels for the spectrum of neutral neon. J. Phys. Chem. Ref. Data 35, 1113–1119. https://doi.org/10.1063/1.2204960.
Schoeninger, M.J., DeNiro, M.J., 1984. Nitrogen and carbon isotopic composition of bone collagen from marine and terrestrial animals. Geochim. Cosmochim. Acta 48, 625–639.
Scott, G.R., Poulson, S.R., 2012. Stable carbon and nitrogen isotopes of human dental calculus: a potentially new non-destructive proxy for paleodietary analysis. J. Archaeol. Sci. 39, 1388–1393. https://doi.org/10.1016/j.jas.2011.09.029.
Shah, F.A., 2020. Towards refining Raman spectroscopy-based assessment of bone composition. Sci. Rep. 10, 16662. https://doi.org/10.1038/s41598-020-73559-2.
Snoeck, C., Lee-Thorp, J., Schulting, R., Jong, J., Debouge, W., Mattielli, N., 2015. Calcined bone provides a reliable substrate for strontium isotope ratios as shown by an enrichment experiment. RCM 29, 107–114. https://doi.org/10.1002/rcm.7078.
Sponheimer, M., Lee-Thorp, J.A., 2006. Enamel diagenesis at South African Australopith sites: Implications for paleoecological reconstruction with trace elements. Geochim. Cosmochim. Acta 70, 1644–1654. https://doi.org/10.1016/j.gca.2005.12.022.
Suarez, C.A., Kohn, M., 2020. Caught in the act: a case study on microscopic scale physicochemical effects of fossilization on stable isotopic composition of bone. Geochim. Cosmochim. Acta 268, 277–295. https://doi.org/10.1016/j.gca.2019.10.008.
Suarez, C.A., Macpherson, G.L., González, L.A., Grandstaff, D.E., 2010. Heterogeneous rare earth element (REE) patterns and concentrations in a fossil bone: implications for the use of REE in vertebrate taphonomy and fossilization history. Geochim. Cosmochim. Acta 74, 2970–2988. https://doi.org/10.1016/j.gca.2010.02.023.
Tacail, T., Le Houedec, S., Skulan, J.L., 2020. New frontiers in calcium stable isotope geochemistry: perspectives in present and past vertebrate biology. Chem. Geol. 537, 119471 https://doi.org/10.1016/j.chemgeo.2020.119471.
Tanabe, K., Hiraishi, J., 1980. Correction of finite slit width effects on Raman line widths. Spectrochim. Acta A 36, 341–344. https://doi.org/10.1016/0584-8539(80)80141-3.
Taylor, L.D., O'Dea, A., Bralower, T.J., Finnegan, S., 2019. Isotopes from fossil coronulid barnacle shells record evidence of migration in multiple Pleistocene whale populations. PNAS 116, 7377–7381. https://doi.org/10.1073/pnas.1808759116.
Thomas, D.B., Fordyce, R.E., Russell, D.F., Gordon, K.C., 2007. A rapid, non-destructive method of detecting diagenetic alteration in fossil bone using Raman spectroscopy. J. Raman Spectrosc. 38, 1533–1537. https://doi.org/10.1002/jrs.1851.
Thomas, D.B., Chinsamy, A., Conard, N.J., Kandel, A.W., 2012. Chemical investigation of mineralisation categories used to assess taphonomy. Palaeogeogr. Palaeoclimatol. Palaeoecol. 361-362, 104–110. https://doi.org/10.1016/j.palaeo.2012.08.011.
Trueman, C.N., 2013. Chemical taphonomy of biomineralized tissues. Paleontology 56, 475–486. https://doi.org/10.1111/pala.12041.
Trueman, C.N., Tuross, N., 2002. Trace elements in recent and fossil bone apatite. Rev. Mineral. Geochem. 48, 489–521. https://doi.org/10.2138/rmg.2002.48.13.
Trueman, C.N.G., Behrensmeyer, A.K., Tuross, N., Weiner, S., 2004. Mineralogical and compositional changes in bones exposed on soil surfaces in Amboseli National Park, Kenya: diagenetic mechanisms and the role of sediment pore fluids. J. Archaeol. Sci. 31, 721–739. https://doi.org/10.1016/j.jas.2003.11.003.
Trueman, C.N., Behrensmeyer, A.K., Potts, R., Tuross, N., 2006. High-resolution records of location and stratigraphic provenance from the rare earth element composition of fossil bones. Geochim. Cosmochim. Acta 70, 4343–4355. https://doi.org/10.1016/j.gca.2006.06.1556.
Trueman, C.N., Privat, K., Field, J., 2008. Why do crystallinity values fail to predict the extent of diagenetic alteration of bone mineral? Palaeogeogr. Palaeoclimatol. Palaeoecol. 266, 160–167. https://doi.org/10.1016/j.palaeo.2008.03.038.
Trueman, C.N., Kocsis, L., Palmer, M.R., Dewdney, C., 2011. Fractionation of rare earth elements within bone mineral: a natural cation exchange system. Palaeogeogr. Palaeoclimatol. Palaeoecol. 310, 124–132. https://doi.org/10.1016/j.palaeo.2011.01.002.
Turner-Walker, G., 2011. The mechanical properties of artificially aged bone: probing the nature of the collagen-mineral bond. Palaeogeogr. Palaeoclimatol. Palaeoecol. 310, 17–22. https://doi.org/10.1016/j.palaeo.2011.03.024.
Turner-Walker, G., Peacock, E., 2008. Preliminary results of bone diagenesis in Scandinavian bogs. Palaeogeogr. Palaeoclimatol. Palaeoecol. 266 (3–4), 151–159. https://doi.org/10.1016/j.palaeo.2008.03.027.
Tuschel, D., 2016. Photoluminescence spectroscopy using a Raman spectrometer. Spectroscopy 31, 14–21.
Tütken, T., 2014. Isotope compositions (C, O, Sr, Nd) of vertebrate fossils from the Middle Eocene oil shale of Messel, Germany. Implications for their taphonomy and palaeoenvironment. Palaeogeogr. Palaeoclimatol. Palaeoecol. 416, 92–109. https://doi.org/10.1016/j.palaeo.2014.08.005.
Tütken, T., Vennemann, T.W., 2011. Fossil bones and teeth. Preservation or alteration of biogenic compositions? Palaeogeogr. Palaeoclimatol. Palaeoecol. 310, 1–8. https://doi.org/10.1016/j.palaeo.2011.06.020.
Tütken, T., Vennemann, T.W., Pfretzschner, H.-U., 2011. Nd and Sr isotope compositions in modern and fossil bones - proxies for vertebrate provenance and taphonomy. Geochim.Cosmochim. Acta 75, 5951–5970. https://doi.org/10.1016/j.gca.2011.07.024.
Tzaphlidou, M., Chapman, J.A., Al-Samman, M.H., 1982. A study of positive staining for electron microscopy using collagen as a model system—II. Staining by uranyl ions. Micron 13 (2), 133–145. https://doi.org/10.1016/0047-7206(82)90080-2.
Voigt, M., Mavromatis, V., Oelkers, E.H., 2017. The experimental determination of REE partition coefficients in the water-calcite system. Chem. Geol. 462, 30–43. https://doi.org/10.1016/j.chemgeo.2017.04.024.
Volesky, B., Holan, Z.R., 1995. Biosorption of heavy metals. Biotechnol. Prog. 11 (3), 235–250. https://doi.org/10.1021/bp00033a001.
Waite, E.R., Child, A.M., Craig, O.E., Collins, M.J., Gelsthorpe, K., Brown, T.A., 1997. A preliminary investigation of DNA stability in bone during artificial diagenesis. Bull. Soc. Géol. Fr. 168 (5), 547–554.
Wang, Y., Cerling, T.E., 1994. A model of fossil tooth and bone diagenesis: Implications for paleodiet reconstruction from stable isotopes. Palaeogeogr. Palaeoclimatol. Palaeoecol. 107, 281–289. https://doi.org/10.1016/0031-0182(94)90100-7.
Weber, K., Weber, M., Menneken, M., Kral, A.G., Mertz-Kraus, R., Geisler, T., Vogl, J., Tütken, T., 2021. Diagenetic stability of non-traditional stable isotope systems (Ca, Sr, Mg, Zn) in tooth enamel – an in-vitro alteration experiment of biogenic apatite in isotopically enriched tracer solution. Chem. Geol. 572, 120196 https://doi.org/10.1016/j.chemgeo.2021.120196.
Williams, C.T., Henderson, P., Marlow, C.A., Molleson, T.I., 1997. The environment of deposition indicated by the distribution of rare elements in fossil bones from Olduvai Gorge, Tanzania. Appl. Geochem. 12, 537–547.
Zhu, Y., Zhang, X., Chen, Y.D., Xie, Q., Lan, J., et al., 2009. A comparative study on the dissolution and solubility of hydroxylapatite and fluorapatite at 25°C and 45°C. Chem. Geol. 268, 89–96. https://doi.org/10.1016/j.chemgeo.2009.07.014.